Received: 2 May 2023 | Revised: 25 November 2023 | Accepted: 29 November 2023

DOI: 10.1002/esp.5758

RESEARCH ARTICLE

ESPL WILEY

Mangrove forest drag and bed stabilisation effects on intertidal flat morphology

Rik Gijsman[1] | Erik M. Horstman[1] | Andrew Swales[2] | Iain T. MacDonald[2] | Tjeerd J. Bouma[3,4] | Daphne van der Wal[4,5] | Kathelijne M. Wijnberg[1]

[1]Coastal Systems and Nature-Based Engineering, Faculty of Engineering Technology, University of Twente, Enschede, The Netherlands

[2]Coastal and Estuarine Physical Processes Group, National Institute of Water and Atmospheric Research, Hamilton, New Zealand

[3]Department of Physical Geography, Utrecht University, Utrecht, The Netherlands

[4]Department of Estuarine and Delta Systems, NIOZ Royal Netherlands Institute for Sea Research, Yerseke, The Netherlands

[5]Department of Water Resources, Faculty of Geo-Information Science and Earth Observation, University of Twente, Enschede, The Netherlands

Correspondence
Rik Gijsman, Coastal Systems and Nature-Based Engineering, Faculty of Engineering Technology, University of Twente, Enschede, The Netherlands.
Email: r.gijsman@utwente.nl

Funding information
Dutch Research Council, Grant/Award Number: 15899; NIWA Strategic Science Investment Fund, Grant/Award Numbers: CECE2304, FWCE2104, FWCE2204; Royal Society of New Zealand's Marsden Fund, Grant/Award Number: 14-UOW-011

Abstract

Mangrove trees influence their physical environment by exerting drag on tidal flows and waves while also stabilising the sediment bed of intertidal flats. These processes influence sediment accretion, the mangrove habitat and their resilience to sea level rise. However, little is known about the magnitude and spatial extent of the effects of mangrove forests on sediment transport and the morphology of the intertidal flat. We use manipulated simulations with an extended process-based numerical model, to study the influence of mangrove forests on intertidal flat morphology on a yearly timescale. The model includes the influence of mangrove trees on tidal flows, waves and sediment dynamics. The model is calibrated and validated with a comprehensive set of measurement data including hydrodynamics, sediment transport and morphological processes from an expanding mangrove forest in the sediment-rich Firth of Thames estuary in Aotearoa New Zealand.

Sediment accretion on the upper intertidal flat is predominantly influenced by the characteristic morphology of the established mangrove forest, with increased bed stability at higher mudflat elevations related to prolonged aerial exposure and drying of the bed. Our results show that, in comparison to the situation without mangroves, sediment accretion increases in the most seaward fringe area of the forest. The unvegetated intertidal flat fronting the mangrove forest captures less sediment compared to the situation without mangroves. The mangrove forest drag triggers the development of a steeper, convex-up-shaped, upper intertidal flat profile, especially during periods with higher water levels and waves. These effects are expected to influence the development and storm-recovery of natural and restored mangrove forests and may contribute to the resilience and persistence of mangrove-vegetated intertidal flats for coastal flood risk reduction.

KEYWORDS
ecosystem engineering, flood risk reduction, mangrove forests, nature-based solutions, persistence, resilience

1 | INTRODUCTION

Mangroves influence their physical environment and thereby can provide a suitable habitat for continued ecosystem development. The majority of (sub)tropical mangrove forests occupy sediment-rich upper intertidal flats on muddy shorelines (Worthington et al., 2020). During high tides, mangroves' stems, branches and aerial roots (i.e., above-ground biomass) induce drag on tidal flows and waves (Mazda & Wolanski, 2009; Mullarney et al., 2017), while their sub-aerial roots (i.e., below-ground biomass) enhance the sediment stability of the bed (Krauss et al., 2003). These biophysical interactions provide a variety of ecosystem services, such as the provision of shelter for fish and

shellfish, the sequestration of carbon, the mitigation of coastal erosion and the reduction of coastal flood risk for adjacent areas (Carrasquilla-Henao & Juanes, 2017; Ezcurra et al., 2016; Temmerman et al., 2023). For a broader implementation of mangrove forests in coastal flood risk reduction, it is essential to develop a quantitative understanding of the ecosystem engineering capacities of mangroves, as they influence the development, resilience and persistence of mangrove ecosystems to future environmental change, including sea level rise (SLR) (Gijsman et al., 2021).

Sediment deposition inside mangrove forests, stimulated by the attenuation of tides and waves, increases with hydroperiod (i.e., frequency and duration of tidal inundation), sediment availability and tree density (Adame et al., 2010; Horstman et al., 2015; Huxham et al., 2010; Lovelock et al., 2015). This feedback allows mangrove forests to vertically grow with SLR (Krauss et al., 2014; Woodroffe et al., 2016). In upper intertidal areas, flood tides can enter mangrove forests rapidly (i.e., sheet flow), whereas the ebb tides have lower peak velocities due to the induced mangrove forest drag (Horstman et al., 2015; Horstman et al., 2021). Upper intertidal flats and mangrove-vegetated areas therefore typically exhibit a flood-dominant peak velocity asymmetry and show a net import of sediment. On mangrove-vegetated upper intertidal flats, sediment deposition occurs because (1) the sediment carrying capacity of the water reduces due to the less-energetic flow and waves, (2) the sluggish ebb-flows are unable to re-entrain sediment that is deposited during high slack tide and (3) the settling velocity of the sediment increases due to flocculation (Furukawa & Wolanski, 1996).

Despite the insights obtained from studies regarding how hydrodynamics and morphodynamics are affected inside mangrove forests (Furukawa & Wolanski, 1996; Mazda et al., 2006; Horstman et al., 2015), much less is known about their effects at ecosystem scales (i.e., exceeding the forest scale). For example, mangroves can improve environmental conditions on nearby coral reefs and seagrass meadows by trapping sediment, reducing turbidity and increasing light penetration (Gillis et al., 2014; Van de Koppel et al., 2015). However, it remains unknown whether, on what timescales, and in which environmental settings mangroves (1) are active colonisers that contribute to their own seaward expansion or reduced landward retreat through ecosystem engineering or (2) are passive colonisers that have limited influence on sedimentation, intertidal flat development and resulting seaward expansion or landward retreat, but instead fully depend on physical processes and intertidal flat morphology (Glover et al., 2022; Proisy et al., 2009; Swales et al., 2015; Van Bijsterveldt et al., 2020, 2023). As a result, little is known about how mangrove ecosystems may respond to SLR and/or reduced sediment availability in terms of cross-shore ecosystem expansion or retreat.

This study aims to quantify the influence of mangrove forests on tidal flows, waves, sediment transport and resulting intertidal flat morphology. More specifically, we determine (1) the cross-shore extent of the influence of mangrove forests as ecosystem engineers, (2) how the magnitude and scale of this ecosystem engineering depends on hydrodynamic and sediment transport processes and (3) the relative contribution of hydrodynamic drag (due to above-ground biomass) and bed stabilisation (due to below-ground biomass) induced by mangrove trees to these ecosystem engineering effects.

The role of mangrove forests in the geomorphic development of upper-intertidal flats is investigated along a cross-shore transect of an expanding mangrove forest in the southern Firth of Thames estuary, Aotearoa New Zealand. We use an extended biophysical process-based numerical model, that incorporates the influence of mangrove vegetation on tides, waves and sediment dynamics at the bed. The model is calibrated and validated against a comprehensive set of field measurement data of hydrodynamic, sediment transport and morphological processes. Manipulated numerical model simulations are used to develop a conceptual understanding of mangrove ecosystem engineering effects on hydrodynamics and morphology along a cross-shore profile.

2 | METHODOLOGY

2.1 | Study site and available data

The Firth of Thames estuary (hereafter Firth) is a large mesotidal estuarine embayment in the upper North Island of Aotearoa New Zealand. The Piako and Waihou rivers are the major source of fluvial sediment which discharge an estimated 190,000 tons of sediment annually to the system (Swales et al., 2015). Along the Firth's southern shoreline, an alongshore-uniform ~1 km wide mangrove forest (*Avicennia marina* var. *australasica*) colonised the upper intertidal area over the last 70 years (Figure 1a; Figure 2). The sediment deposited on the intertidal flat consists of clay (~35%), silt (~60%) and sand (~5%), with a median grain size (D_{50}) of 6.4–8.9 μm and an organic matter content (OC) of approximately 10% (Nguyen et al., 2019, 2020). The upper intertidal and mangrove-vegetated platform has been expanding seaward, with long-term ^{210}Pb sediment accretion rates of ~3 cm/year on the unvegetated mudflat, ~2–5 cm/year in the forest fringe and ~1 cm/year in the mature forest (Swales et al., 2015). Measurements at rod surface elevation table (RSET) sites show that sediment accretion is counteracted by shallow subsidence due to compaction of 0.4–1.6 cm/year and deep subsidence of ~1 cm/year of the sedimentary basin (Swales et al., 2016, 2019).

The density and height of the mangrove trees vary along the cross-shore profile with maximum values of 12 stems/m^2 and 3.8 m, respectively (Figure 1b; Horstman et al., 2018). The cross-shore variation developed because of the long-term mudflat accretion in combination with large-scale seedling establishment events (i.e., ~100 + m cross-shore) that were triggered by rare calm-weather periods (Lovelock et al., 2010; Swales et al., 2015). The development of the mangrove ecosystem created distinct cross-shore zones in the forest, starting with the most seaward unvegetated mudflat, through a dynamic area just seaward of the upper intertidal platform where seedlings are establishing (i.e., the seedling establishment zone), a dynamic forest fringe on the seaward slope of the upper intertidal platform and the scrub and relict fringe forest at the landward extent of the platform (Figure 1c; Figure 2; Swales et al., 2015, 2019). In this study, the mangrove forest edge is defined as the seaward side of the present-day dynamic forest fringe.

A decadal-timescale dataset of environmental parameters has been collected in the southern Firth. Water levels are recorded at the Tararu tidal gauge (*Waikato Regional Council, site nr. 1033.1*). A climate station at the stop bank, immediately landward of the mangrove forest (*NIWA climate station 38,619*) collects wind, temperature and pressure data (Figure 1a). In addition, intermittent datasets of hydrodynamics, morphology and vegetation characteristics (e.g., Balke et al., 2015; Horstman et al., 2018; Lovett, 2017; Tablada Torres, 2020) as well as cross-shore surveys of the profile elevation

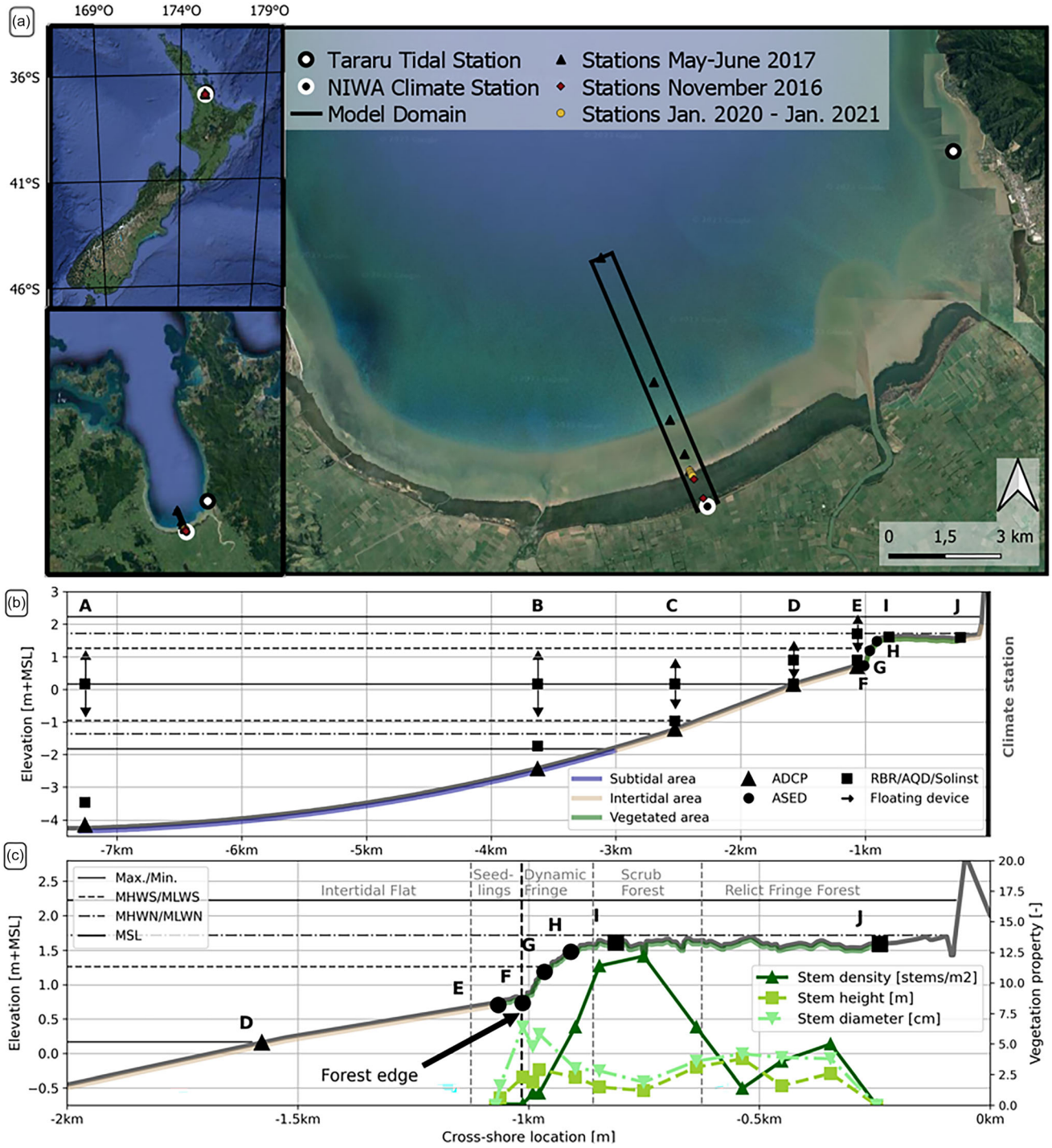

FIGURE 1 An overview of the study site and field measurement stations used for this study. (a) The Firth of Thames estuary and mangrove forest in Aotearoa New Zealand on different scales including measurement stations and model domain. (b) The cross-shore profile along the subtidal and intertidal area until the stopbank, including the fixed and floating measurement stations. (c) The cross-shore bathymetry of the upper intertidal flat platform with measurement stations, vegetation characteristics and vegetation zones (data from Horstman et al., 2018). [Color figure can be viewed at wileyonlinelibrary.com]

(in 2005, 2016 and 2022) and soil shear strength (in 2022) were collected in the Firth (Horstman et al., 2018; Swales et al., 2015).

2.2 | Field measurements and data treatment

This study used three field measurement campaigns that were carried out in the Firth in the periods of May–June 2017, November 2016 and January 2020–January 2021 (Figure 1a). During the field campaign of May–June 2017, hydrodynamics and sediment transport were measured in the shallow subtidal and intertidal area (station A-E in Figure 1b). Stations A-E were equipped with Acoustic Doppler Current Profilers (ADCPs) and RBR Concerto's on a bedframe (~0.2 m above bed) as well as on a floater (~0.2 m below the water surface). At these stations, current profiles, pressure and turbidity were measured at 10-minute burst intervals. Burst-median current profiles were decomposed into an alongshore and a cross-shore component and then depth-averaged. Pressure readings were corrected for the atmospheric pressure (measured at the climate station) and burst-averaged spectral wave heights (H_{m0}) and mean periods (T_{m01}) were then

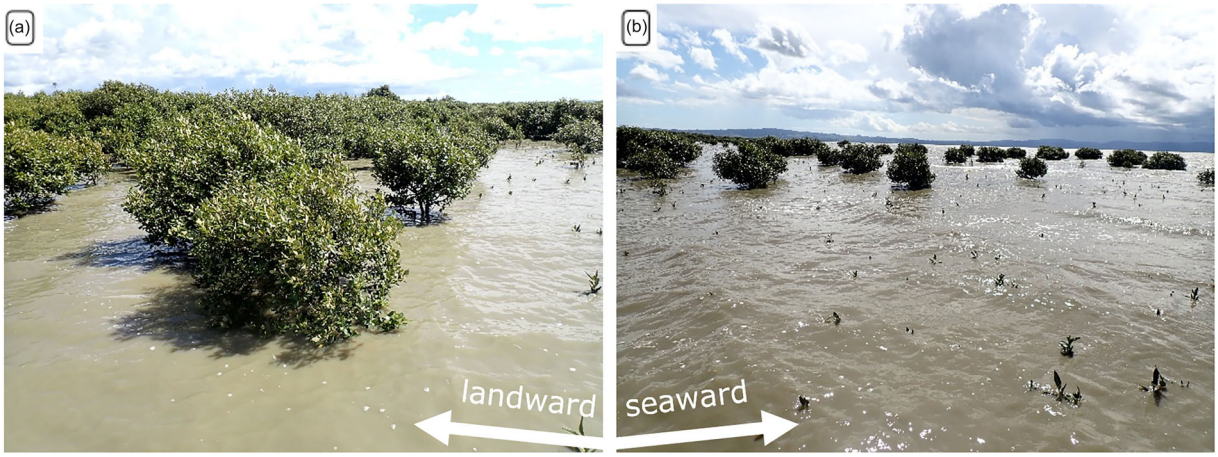

FIGURE 2 The Firth mangrove forest in the zone spanning the transition from the seedling establishment zone to the dynamic forest fringe. Photos taken at the forest edge location (indicated in Figure 1c) and looking in alongshore direction (a) with slight turn landward to look at the dynamic fringe area and (b) with slight turn seaward to look at the seedling establishment zone. Photo credit: R. Gijsman, 20 December 2022. [Color figure can be viewed at wileyonlinelibrary.com]

determined using a spectral analysis method following Horstman et al. (2014). Observed burst-median turbidity was converted to *SSC* following a lab calibration for each instrument (polynomial fits with min. $r^2 = 0.967$), and then depth-averaged ($\overline{SSC}$).

In November 2016 wave attenuation in the mangrove forest was measured at stations E-J (Figure 1; Montgomery et al., 2018, 2019). Pressure data was sampled at stations E, I and J with a Nortek Aquadopp, RBR Duet and Solinst Levelogger, respectively (Montgomery et al., 2018). Pressure readings were corrected for atmospheric pressure and temperature and converted to water depth. H_{m0} was calculated following Horstman et al. (2014) at stations E and I. Water depth was burst-averaged (10-minute intervals) at stations E and I and measured continuously at station J (1-minute interval).

The January 2020–January 2021 measurements quantified surface accretion/erosion in the dynamic mangrove forest fringe (station E-H in Figure 1c). Surface elevations were measured using Acoustic Surface Elevation Dynamics (NIOZ ASEDs) sensors. The sensors measured in 15-minute interval bursts, comprising 10 sound readings. Provided that the sensor was inundated, bed surface elevation was determined following Willemsen, Horstman, et al. (2022). Inundation was detected when the signal intensity in the expected bed level range (i.e., 0.15–0.3 m from the instrument) was larger than the signal intensity in the expected noise range (i.e., 0–0.15 m from the instrument). Any remaining signal noise was removed from the data using the water levels recorded at the Tararu tidal gauge, in comparison to the acoustic-sensor elevation. The reflection time was defined as the time at which the smoothened signal intensity started to increase to its maximum value. A threshold of 10% of the maximum signal intensity was used for the identification of the bed. The distance to the bed was then determined by dividing the reflection time by the speed of sound in sea water (1,500 m/s). Burst median values of the ASED measurements were used for further analysis and bursts with a standard deviation greater than 5 mm were omitted.

2.3 | Model setup

A 2D depth-averaged hydro- and morphodynamic process-based model was setup in Delft3D Flexible Mesh (Deltares, 2022a), and applied to the cross-shore elevation gradient in the southern Firth (Figure 1a; Figure 3). This approach has been adopted in recent numerical modelling studies in vegetated intertidal environments (e.g., Willemsen, Smits, et al., 2022; Xie et al., 2020, 2022). The present study included variability in the sediment bed stability of the intertidal flat due to aerial exposure (e.g., drying and/or biofilm presence) following Nguyen et al. (2020), who found that longer periods of aerial exposure lead to sustained increases in sediment bed stability (Fagherazzi et al., 2017; Nguyen et al., 2022). The present study also included the effects of mangrove trees on tides, waves and sediment dynamics.

Hydrodynamic flow propagation was computed with a continuity and momentum balance, while wave propagation was computed with a wave energy balance. The model had a cross-shore length of 7,300 m in the x-direction and an alongshore width of 300 m in the y-direction for hydrodynamic flow (i.e., flow velocities) and sediment transport simulations (Figure 3). For the wave domain, the model width was increased to 600 m to avoid boundary effects in the flow domain. An alongshore uniform bathymetry was imposed based on cross-shore bathymetric surveys. Zero Neumann boundaries were applied at the alongshore boundaries of the flow domain. Grid cells of the flow domain varied from 20mx20m in the offshore area to 10mx10m near and within the dynamic mangrove fringe (Figure 3). The waves were resolved on a spatially homogeneous grid of 25mx25m. While hydrodynamic flow and sediment transport were computed on a Courant-number limited timestep of a maximum 2 minutes, waves were computed with a wave computation interval of 15 minutes.

Damping of flows (i.e., reduction of flow momentum) and attenuation of waves (i.e., reduction of wave energy) by the mangrove trees was imposed following Baptist et al. (2007) and Mendez & Losada (2004), respectively. These computations require inputs regarding the dimensions and density of vegetation elements. The tree height (H) and density (d) along the cross-shore profile were obtained from field measurements (Figure 1c) and converted to a tree cover. Following previous mangrove growth models (e.g., Chen & Twilley, 1998; Berger & Hildebrandt, 2000), a fixed allometric relation between the stem diameter (D) of the trees and the tree height was derived following a power-law fit to measurement data of Horstman et al. (2018) ($H = a \cdot D^b$, with $a = 14.72$ and $b = 0.58$, $p < 0.05$, $r^2 = 0.37$).

Suspended sediment transport was calculated with an advection–diffusion equation (Deltares, 2022b). Sediment exchange with the bed was computed with the formulations of Partheniades-Krone

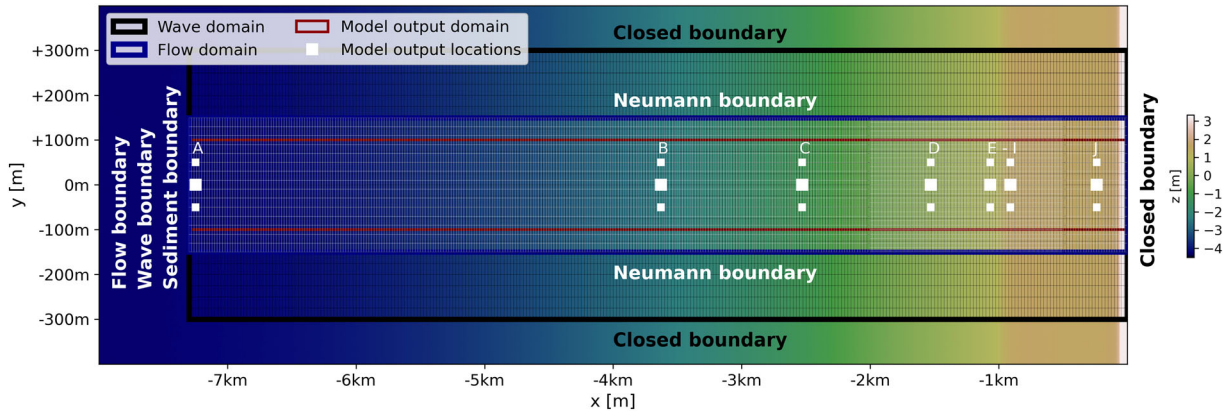

FIGURE 3 Model setup with wave and flow domain, boundary conditions, bathymetry, output domain and output locations A to J in model centre ($y = 0$ m) and 50 m in both alongshore directions ($y = \pm 50$ m). [Color figure can be viewed at wileyonlinelibrary.com]

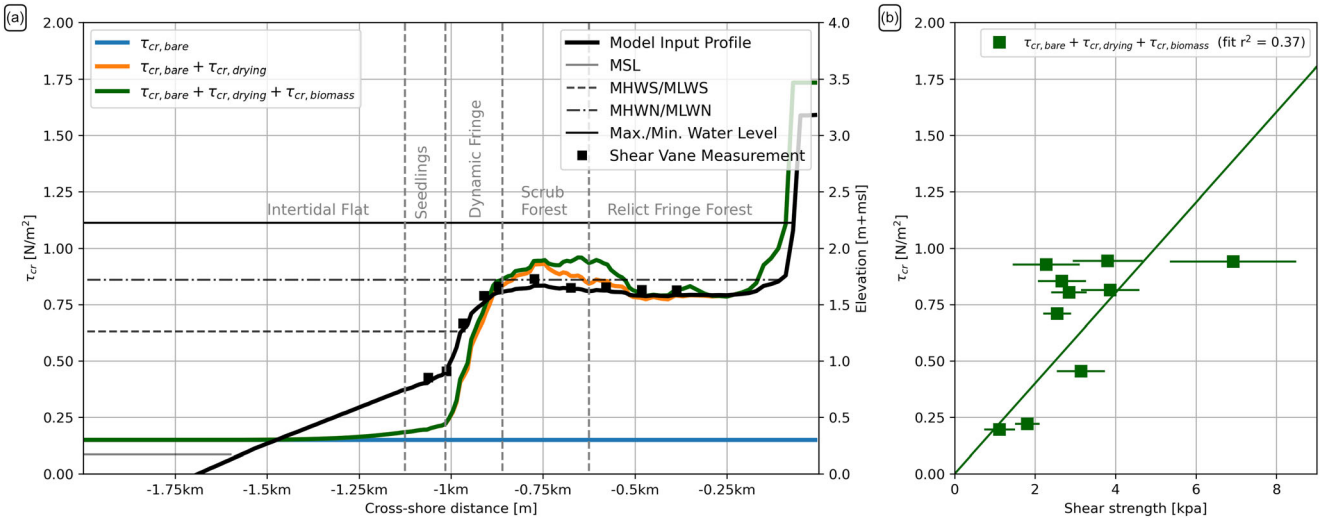

FIGURE 4 The imposed critical bed shear stress for erosion and a comparison to measured soil shear strengths in the Firth. (a) The critical bed shear stress contributions of the bare mudflat, drying due to aerial exposure and biomass along the profile of the Firth. The model input bathymetry, tidal water levels, the mangrove forest zones and the locations of the shear strength measurements are indicated. (b) The comparison between the soil shear strength (mean and standard deviation) measured along the profile in the Firth with a Humboldt H-4212MH pocket shear vane tester in December 2022, and the critical bed shear stress for erosion (equation 1) based on the elevation of these measurements and the mangrove biomass at these locations. [Color figure can be viewed at wileyonlinelibrary.com]

(Partheniades, 1965) for cohesive-sediment transport. Deposition occurred depending on the sediment settling velocity (w_s) and the local suspended sediment concentration (*SSC*). Erosion of the bed occurred at a rate specified by the erosion parameter (M) if the combined wave-current bed shear stress (τ_{cw}) exceeded a critical erosion threshold (τ_{cr}).

In the present study, τ_{cr} included three components: (1) a background value for the bare subtidal and intertidal mudflat that is submerged daily ($\tau_{cr,bare}$), (2) the reduced erodibility of the intertidal mudflat due to intermittent aerial exposure ($\tau_{cr,drying}$) and (3) the stabilising contribution of mangrove biomass ($\tau_{cr,biomass}$):

$$\begin{aligned} \tau_{cr} &= \tau_{cr,bare} + \tau_{cr,drying} + \tau_{cr,biomass} \\ \tau_{cr,drying} &= c_1 z^{c2}, \text{for } 0 < z < 2 \\ \tau_{cr,biomass} &= c_3 \left(B/B_{max}\right) \end{aligned} \quad (1)$$

In Equation (1), $\tau_{cr,bare}$ was determined following a model calibration (Section 2.4). For $\tau_{cr,drying}$, z was the bed level elevation relative to mean sea level (m + msl) and coefficients c_1 (0.106 N/m^3) and c_2 (3.898) were determined from the study of Nguyen et al. (2020) in the Firth, in combination with the mean exposure duration of the intertidal area based on the Tararu tidal gauge water levels from 2017 (Figure 4; Supporting Information S1). For $\tau_{cr,biomass}$, B was the total mangrove biomass determined by the total mangrove biomass of all trees in a grid cell divided by the surface area of that particular grid cell and B_{max} was the maximum mangrove biomass present in the forest (=202 kg/m^2). The biomass of the trees was computed based on the tree diameter, and the combined above-ground and below-ground biomass following Comley & McGuiness (2005) was interpolated on the model grid. The value of c_3 was set to 0.1 N/m^2 following Van Maanen et al. (2015). τ_{cr} was also compared to soil shear strength measurements collected at the study site (Figure 4b).

Model output was analysed as an alongshore average μ_y (or standard deviation σ_y) selected from a 200 m wide domain in the model centre, to avoid boundary effects on the model results. In addition, output locations were selected based on the instrument

TABLE 1 Model parameters calibrated in the Delft3D flexible mesh model.

Model parameter	Symbol	Unit	Calibration range	Calibration value	Reference
Manning roughness	n	$s/m^{1/3}$	0.015–0.025	0.018	Deltares (2022a)
Wave friction factor for wave dissipation	F_w	m^2/s^3	0.01–0.067	0.018	Deltares (2022c)
Critical bed shear stress for erosion	$\tau_{cr,bare}$	N/m^2	0.1–0.5	0.15	Deltares (2022b); Nguyen et al., (2020)
Erosion parameter	M	kg/m^2s	0.000025–0.000100	0.00004	Deltares (2022b)
Sediment settling velocity	w_s	m/s	0.00025–0.00100	0.0004	Deltares (2022b); Estimated in Swales et al., (2019)
Drag coefficient for wave attenuation	C_D (wave)	-	0–3	3	Re-analysis Montgomery et al., (2018)
Drag coefficient for flow damping	C_D (flow)	-	0–3	3	Re-analysis Montgomery et al., (2018)

locations, both in the model centre ($y = 0$ m) as well as 50 m in each alongshore direction ($y = \pm 50$ m), to analyse spatial variability in the model output.

2.4 | Model calibration

The hydrodynamic and morphodynamic model was calibrated with the field measurement data obtained from May–June 2017 and November 2016. The Manning roughness coefficient of the bed (n), friction factor for wave dissipation (F_w), background value of the critical erosion threshold ($\tau_{cr,bare}$), erosion parameter (M), sediment settling velocity (w_s) and the drag coefficient for flow damping and wave attenuation (C_D) were calibrated against the field measurement data. Calibration ranges were restricted based on previous studies as indicated in Table 1. The calibration procedure was as follows: firstly, n was calibrated by comparing simulated and observed cross-shore flow velocities (u_x). Secondly, F_w was calibrated by comparing simulated and observed spectral wave heights on the unvegetated mudflat (H_{m0}). Thirdly, the C_D coefficients for flow and waves were calibrated by comparing wave attenuation rates in the forest. Lastly, $\tau_{cr,bare}$, M and w_s were calibrated by comparing simulated and observed suspended sediment mass (S) (i.e. SSC multiplied by the water depth). The final parameter values, with the exception of the C_D coefficients, were determined from a quantitative comparison of the model output with the measurements at station D, approximately 500 m seaward from the mangrove forest edge. The C_D coefficients for flow and waves were determined from a comparison of tidal damping between stations E to J and wave attenuation rates between stations E and I, respectively (Supporting Information S2; Montgomery et al., 2018).

The bathymetry for the calibration simulations was imposed based on an RTK-GPS survey (Trimble GNSS) just prior to the hydrodynamic and morphological data collection, in December 2016 (Horstman et al., 2018). Random perturbations up to 2 cm amplitude were introduced to represent undulations of the bed that remained unresolved by the RTK-GPS survey and to avoid delayed morphological responses due to an alongshore flat bed. The calibration simulations were forced at the offshore model boundary with water level data from the Tararu tidal station (Figure 1), a Pierson-Moskowitz (PM) spectrum with measured H_{m0} and T_{m01}, and $\overline{SSC}$ measured at station A.

2.5 | Model validation

With the calibrated settings, the morphodynamic model was validated using high-resolution surface elevation change measurements obtained during the period January 2020-January 2021. The validation was carried out at measurement stations E-H (Figure 1c). Relative bed levels were averaged per tide to determine the longer-term trend in bed level change.

The bathymetry for the validation simulation was imposed from an RTK-GPS bathymetric survey (Trimble GNSS) performed in December 2022. Model validation simulations were also forced with Tararu tidal station water levels. Timeseries of the H_{m0} and T_{m01} of the wave spectra, and $\overline{SSC}$ at the offshore model, boundary were reconstructed for the full validation period. The reconstruction was based on the relations of these parameters with the wind climate (direction and speed) that were obtained for the model calibration period May–June 2017 (Supporting Information S3).

2.6 | Model scenarios

To reveal the effects of drag and bed stabilisation induced by the mangrove forest on the morphology of the intertidal flat, the validated model simulation from January 2020 to January 2021 was repeated with different values of mangrove-induced drag (C_D) and bed stabilisation effects ($\tau_{cr,biomass}$). Moreover, influences of the present morphology were also evaluated by additional model simulations without bed stabilisation due to aerial exposure ($\tau_{cr,drying}$). An overview of the conducted model scenarios with or without influences of mangrove drag (*Drag*), drying (*Drying*) and/or biomass (*Biomass*) is presented in Table 2.

The relative effects of mangrove drag and stabilisation on intertidal flat morphodynamics were investigated by comparing model output from the simulation *with* mangroves (Drag – Drying – Biomass) and the simulation *without* mangroves (~~Drag~~ – Drying – ~~Biomass~~) in three ways. Firstly, the length scales of mangroves' influence on

TABLE 2 Setup of the model scenarios. The scenario names indicate which influences are included and excluded (i.e., strikethrough) from the model simulation. The text colour also indicates whether the influence was included (green text) or excluded (red text) from the model simulation.

Scenario name	Mangrove ecosystem engineering processes	C_D	τ_{cr}
~~Drag~~ ~~Drying~~ ~~Biomass~~	No Mangrove drag No Morphology stabilisation No Mangrove stabilisation	0	τ_{bare}
~~Drag~~ Drying ~~Biomass~~	No Mangrove drag Morphology stabilisation No Mangrove stabilisation	0	$\tau_{bare} + \tau_{drying}$
~~Drag~~ Drying Biomass	No Mangrove drag Morphology stabilisation Mangrove stabilisation	0	$\tau_{bare} + \tau_{drying} + \tau_{biomass}$
Drag Drying ~~Biomass~~	Mangrove drag Morphology stabilisation No Mangrove stabilisation	3	$\tau_{bare} + \tau_{drying}$
Drag ~~Drying~~ Biomass	Mangrove drag No Morphology stabilisation Mangrove stabilisation	3	$\tau_{bare} + \tau_{biomass}$
Drag Drying Biomass	Mangrove drag Morphology stabilisation Mangrove stabilisation	3	$\tau_{bare} + \tau_{drying} + \tau_{biomass}$

surface accretion/erosion were determined based on cumulative surface accretion/erosion differences (i.e., the relative morphological change) with a threshold value of 1 mm. Secondly, the magnitude of mangroves' influence on sediment accretion was considered by comparing the difference in cumulative surface accretion/erosion volume integrated along distinct cross-shore forest zones (Figure 1c). Lastly, we compared tidal surface accretion/erosion volumes for distinct cross-shore forest zones relative to the forcing (i.e., maximum water level and wave height at station E) during each tide, to study the conditions in the mangrove forest for which these morphological effects were most prominent.

3 | RESULTS

3.1 | Measured and modelled hydrodynamics and sediment transport on the subtidal and intertidal flat

The tidal range during the measurement campaign of 2017 varied from 2.0 m to 3.8 m, covering several spring-neap cycles showing a distinct monthly variability (Figure 5a). At the most offshore location, in the subtidal zone (station A in Figure 1), depth-averaged cross-shore flow velocities ($\bar{u}$) up to 0.44 m/s were observed with flood-dominant tidal peak velocities. The mean H_{m0} was 0.19 m (standard deviation [σ] of 0.20 m) and the mean T_{m01} was 4.2 s (σ = 1.6 s) (Figure 5b). H_{m0} increased to a maximum of 1.26 m after strong onshore winds on the 17th of May. During this event, *SSC* at station A showed a large vertical gradient from near-bed to near-surface of 1,188 mg/l to 148 mg/l, and the depth-averaged $\overline{SSC}$ increased substantially (650 mg/l) in comparison to the mean $\overline{SSC}$ of 39.7 mg/l (σ = 44.8 mg/l) for the full measurement campaign (Figure 5b). $\overline{SSC}$ values remained high throughout the tidal cycles on the 17th and 18th of May (Figure 5b), and the observed strong ebb flows caused substantial offshore suspended sediment transport. While the event caused offshore transport of suspended sediment, spring tidal conditions steered suspended sediment transport onshore due to the flood-dominant tidal flow velocities in combination with a higher $\overline{SSC}$ in the flood phase.

On the intertidal flat between stations A and E, the wave height attenuation per metre distance increased linearly with H_{m0} ($r^2 = 0.96$), yielding a wave attenuation rate of 1.35×10^{-4} m^{-1}. Cross-shore flow velocities reduced onshore to a maximum of 0.27 m/s (at station D) and became ebb dominant (Figure 5e). On the intertidal flat, *SSC* became well mixed within the water column. $\overline{SSC}$ values at station D increased to a maximum of 2,375 mg/l (μ = 167 mg/l, σ = 505 mg/l). While simulated cross-shore flow velocities were insensitive to the Manning roughness coefficient *n* (set to 0.018 s/m$^{1/3}$, Table 1), simulated wave heights were sensitive to F_w and a value of 0.018 m^2/s^3 yielded the best fit to the data ($p < 0.01$, $r^2 = 0.86$ and a root-mean-squared-error [rmse] = 0.02 m; Figure 5c,d). Simulated water depths ($p < 0.01$, $r^2 = 0.99$, rmse = 0.05 m; Figure 5c) and flow velocities ($p < 0.01$, $r^2 = 0.75$, rmse = 0.05 m/s; Figure 5e) were in good agreement with measurements. The match between modelled and measured suspended mass (*S*) at station D has a p-value below 0.01, r^2 of 0.44 and rmse of 0.17 kg/m^2 (Figure 5e), with an erosion parameter *M* of 0.00004 kg/m^{2}s, a sediment fall velocity w_s of 0.0004 m/s and $\tau_{cr,bare}$ of 0.15 N/m^2 (Figure 5e,f).

In the mangrove-vegetated area, the wave height attenuation rate between stations E and I was $r = 3.8 \times 10^{-3}$ m^{-1} ($r^2 = 0.99$), which was an order of magnitude higher than on the unvegetated intertidal flat. Water level damping between stations E and J exceeded 0.10 m during the largest spring tides (Supporting Information S2; Montgomery et al., 2019). The mangrove vegetation also imposed a delay in high water between stations E and J exceeding 1 hour (Supporting Information S2; Montgomery et al., 2019). A comparison between the measured and modelled wave attenuation and tidal damping yielded a C_D coefficient of 3 for both wave attenuation and water level damping (Table 1).

Variations in *SSC* (and *S*) were driven by tidal flooding and ebbing, the tidal range and the wave height. *SSC* values were typically higher

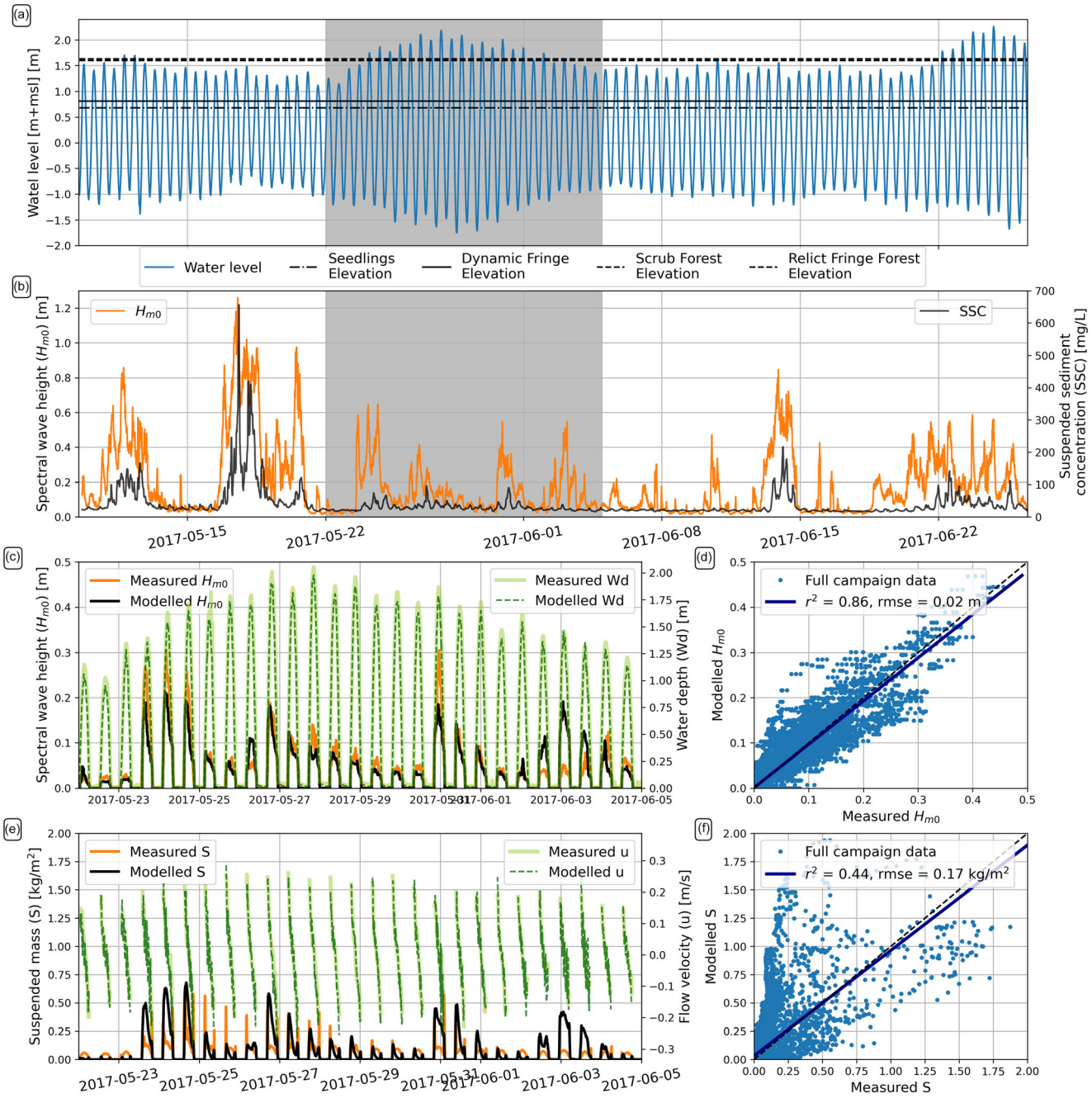

FIGURE 5 Model calibration with field measurement data from May–June 2017. (a) Water levels monitored at station A and boundary forcing for the model. The minimum elevation of the forest zones is indicated. (b) Spectral wave heights and suspended sediment concentrations measured at station A and boundary forcing for the model (c,d) comparison of measured and modelled spectral wave height and water depth for a 14-day period (shaded area in panel (a) and (b)) at station D and fit of the spectral wave height for the full period at station D. (e,f) Comparison of measured and modelled suspended sediment mass and flow velocity for the 14-day period at station D and fit of the suspended mass for the full period at station D. [Color figure can be viewed at wileyonlinelibrary.com]

during the initial stage of the flood tide in comparison to the late ebb tide. This tidal asymmetry in SSC increased with increasing tidal range and flow velocities during spring tides (Figure 5e,f). *SSC* values in the intertidal area were also higher than in the subtidal area.

3.2 | Measured and modelled profile development and sediment accretion

Profile surveys between 2005 and 2022 indicated that the surface elevation of the upper intertidal area has been increasing at rates of up to 4.0 cm/year (between 2005 and 2016) and 3.5 cm/year (between 2016 and 2022) in the dynamic fringe forest (Figure 6a,b). These rates were consistent with high-precision measurements of surface-elevation trends (0.7 to 3.7 cm/year) at RSET stations located across the area (2009–2018, Swales et al., 2019, Figure 5), co-located with the survey profile. At the locations of stations E, F, G and H, the total surface elevation in the profile surveys increased at rates of 0.4 cm/year, 0.8 cm/year, 3.2 cm/year and 2.0 cm/year, respectively (between 2005 and 2022) (Figure 6b). Measured net sediment accretion rates between January 2020 and January 2021 obtained with the ASED sensors were larger at 8.8 cm/year,

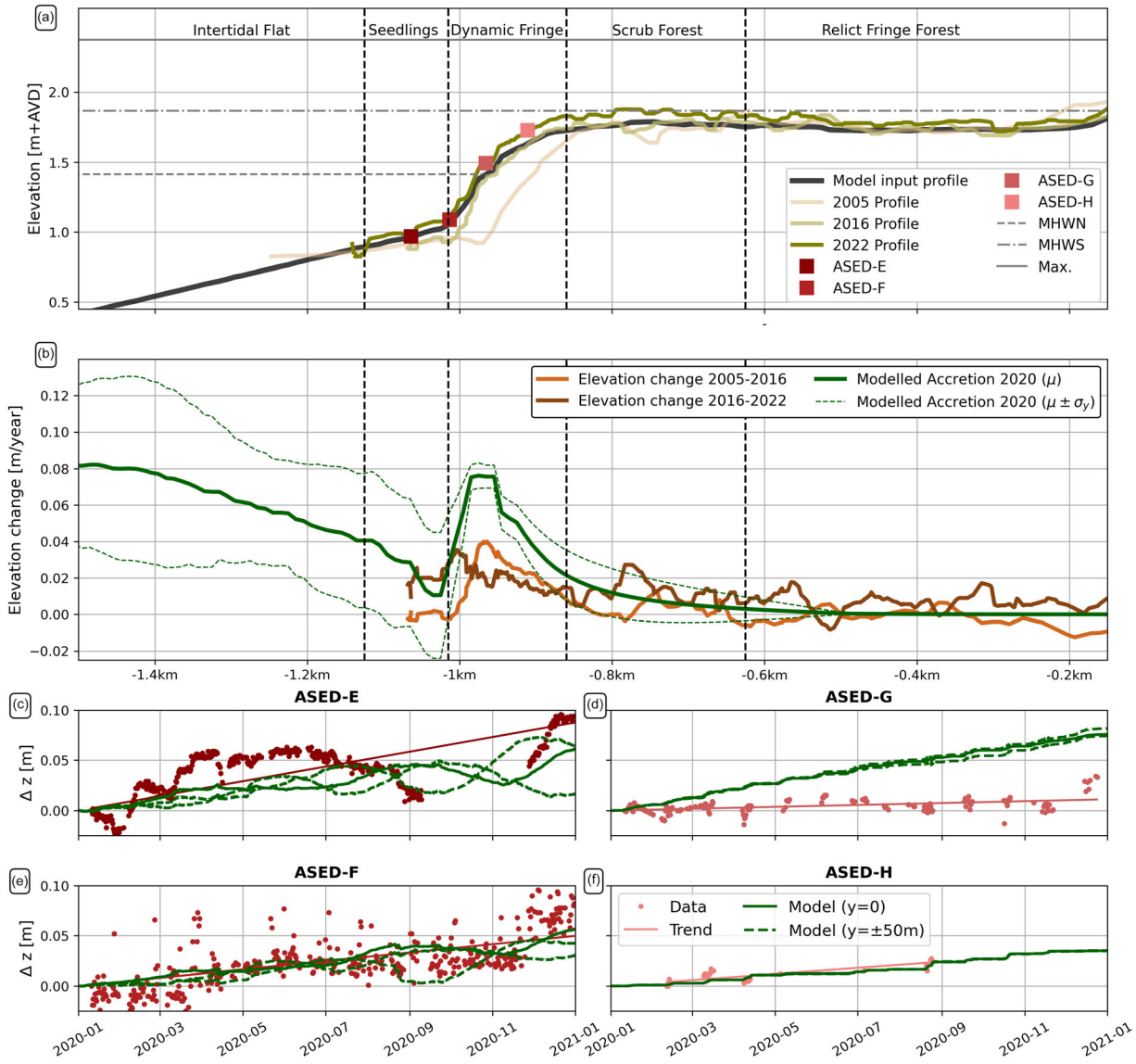

FIGURE 6 Model validation with measured elevation profiles (2005, 2016 and 2022) and field measurement data of January 2020–January 2021. (a) Measured cross-shore profile elevation and the profile imposed for the model simulation. Mangrove forest zones, water levels and locations of ASED sensors shown (b) comparison of measured and modelled cross-shore profile elevation change with alongshore mean and standard deviation. Presented modelled cross-shore elevation changes are median averaged over 20 m. (c-f) Measured elevation change at ASED sites in 2020 including a trend line, and modelled accretion in the model centre and 50 m from the centre in alongshore direction. The overestimated accretion at station G is discussed in Section 4.2. [Color figure can be viewed at wileyonlinelibrary.com]

5.0 cm/year, 1.1 cm/year and 3.6 cm/year at stations E, F, G and H, respectively (Figure 6c–f).

Simulated sediment accretion in the validation run for the year 2020 showed realistic accretion rates increasing up to 7.6 cm/year in the dynamic fringe forest. The model also reproduced the measured reduction in accretion further inland, towards the scrub and relict fringe forest (Figures 6b and 7a). Simulated alongshore-averaged sediment accretion rates at measurement stations E, F, G and H were 2.9 cm/year, 2.6 cm/year, 7.6 cm/year and 4.4 cm/year, respectively. Simulated sediment accretion showed a reduction in alongshore variability (σ_y) in landward direction on the upper intertidal platform in the mangrove forest (Figure 6b). Particularly at stations E and F, the model indicated that accretion rates vary considerably in the alongshore direction. The temporal variability in accretion also reduced rapidly from the most seaward stations E and F towards the higher elevated stations G and H inside the mangrove forest (Figure 6c–f).

3.3 | Modelled ecosystem engineering effects of mangroves

Absolute cumulative accretion volumes in the simulation *with* mangroves were 2.74 m^3/m/year in the seedling establishment zone, 7.97 m^3/m/year in the dynamic forest fringe, 2.04 m^3/m/year in the scrub forest and 0.21 m^3/m/year in the relict fringe forest (Figure 7a). Compared to the situation *without* mangroves, in the dynamic forest fringe, additional accretion of +2.77 m^3/m/year was simulated, and the additional accretion was present over a distance up to 190 m landward of the forest edge (Figure 7b,c). However, the mangrove forest caused a reduction in accretion in the scrub (−0.94 m^3/m/year) and relict fringe forest (−1.76 m^3/m/year), and this reduced accretion effect extended up to 785 m landward from the forest edge. This reduced accretion was caused by a reduced sediment supply because of the drag and bed stabilisation effects of the mangroves. Also, the seedling

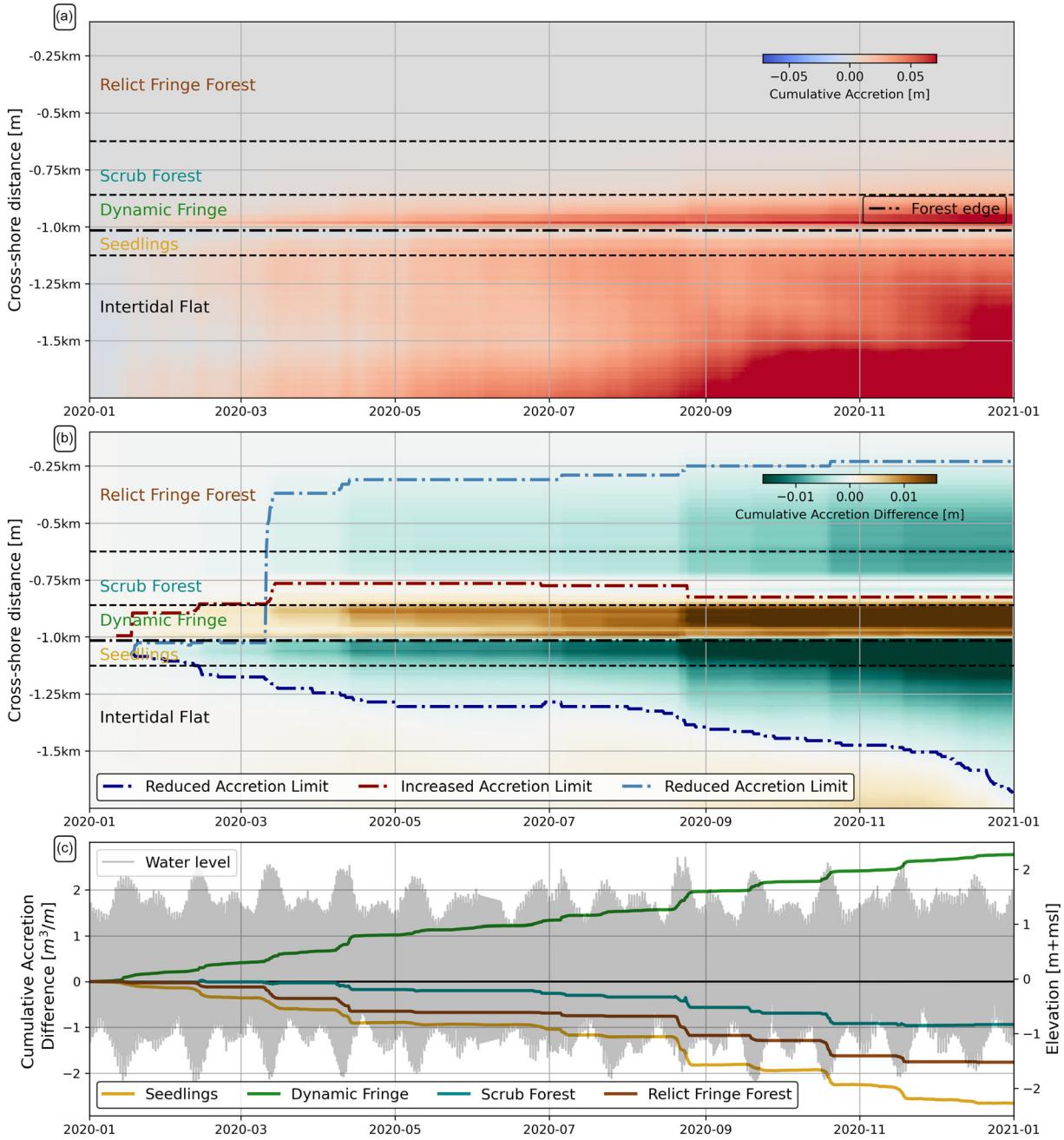

FIGURE 7 Simulated profile accretion (year 2020) and the relative cumulative difference between the simulation *with* (simulation *drag-drying-biomass*) and *without* (simulation ~~*drag-drying-biomass*~~) mangrove forest influence. (a) The alongshore averaged cumulative accretion in space and time for the simulation *with* mangroves with mangrove forest zones indicated. (b) The difference in cumulative alongshore averaged accretion between the simulation *with* mangroves compared to the simulation *without* mangroves in space and time. Cross-shore limits of increased/reduced accretion and mangrove forest zones are indicated. (c) The temporal cumulative difference in accretion volume between the simulation *with* mangroves and the simulation *without* mangroves in different mangrove forest zones. Tidal water level of the Tararu tidal gauge shown in the background. [Color figure can be viewed at wileyonlinelibrary.com]

establishment zone in front of the dynamic fringe received less sediment (−2.66 m^3/m/year) when the mangroves were included. This reduced accretion effect extended up to 670 m seaward of the forest edge by the end of the year, and was initiated by the increased sediment entrainment by the ebb flows that carry relatively little sediment when leaving the forest. The sediment re-entrained by these ebb flows deposited further seaward in the lower intertidal and subtidal area.

The effects of mangroves on tidal sediment deposition were most pronounced during spring tides when the mangrove forest was most deeply inundated (Figures 7c and 8a–d). Wave heights also affected sediment accretion in the forest, with increasing wave heights causing erosion in the mangrove seedling establishment zone (Figure 8a) and additional accretion in the dynamic forest fringe (Figure 8b). The scrub and relict fringe forest only received sediment with the largest tidal inundations and wave heights (Figure 8c,d).

Mangroves' effect on sediment accretion was found to be dominated by mangrove drag, as the magnitude of the tidal accretion difference caused by drag (Figure 8e–h) was larger than the differences caused by the stabilisation effect (Figure 8i–l). Remarkably, in the scrub forest, mangrove drag caused a relative increase in accretion during low wave conditions, but a relative decrease in accretion during high wave conditions (Figure 8g). In the seedling establishment

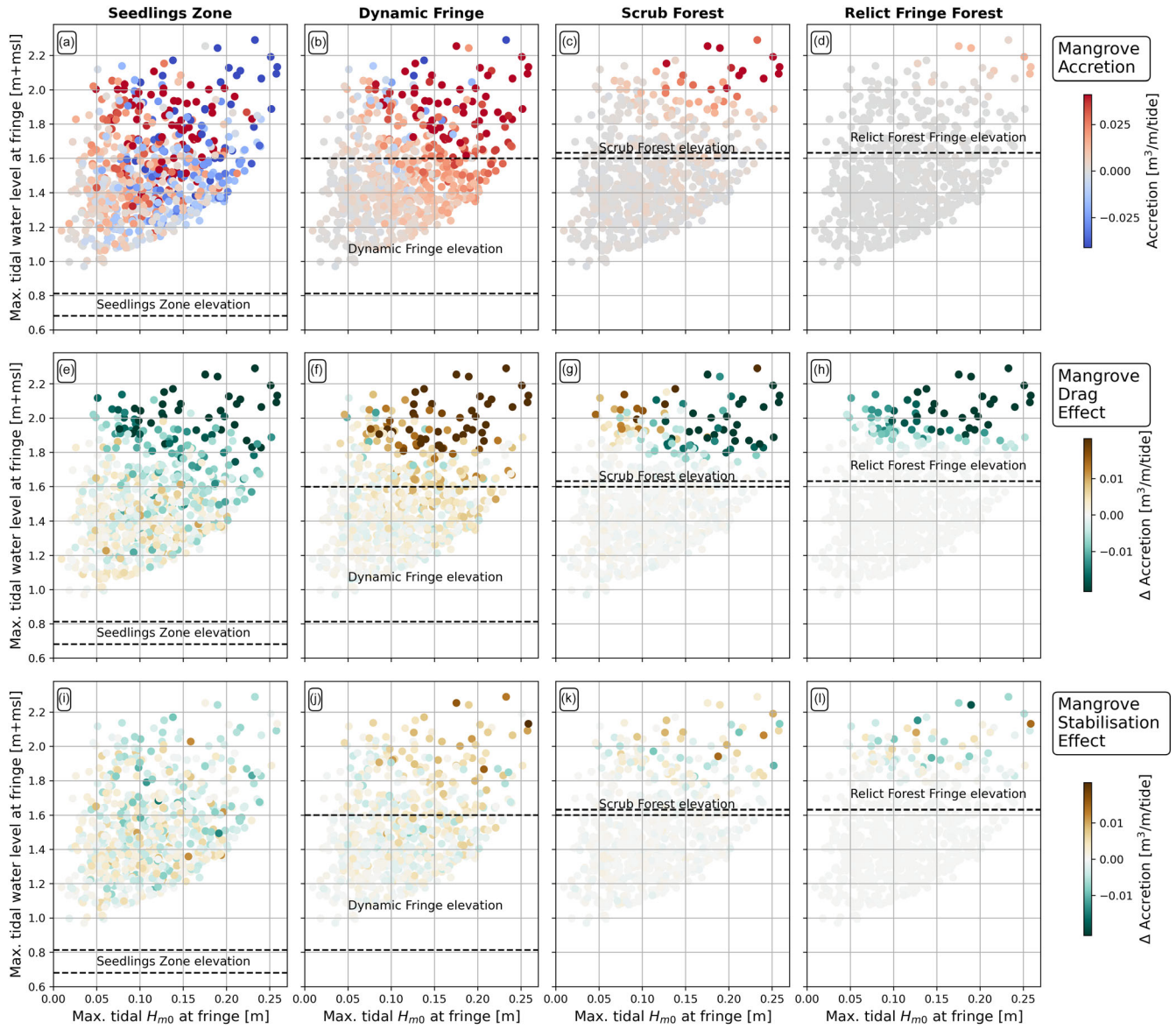

FIGURE 8 Simulated tidal accretion for the year 2020 (each dot represents 1 tide) and the relative tidal accretion based on mangrove effects (Table 2). The tidal accretion and relative tidal accretion difference are plotted as a function of the tidal maximum water level and wave height at the mangrove dynamic fringe forest (station E). The minimum and/or maximum elevation of each forest zone is indicated by the dotted lines. (a-d) Total tidal mangrove accretion (*drag-drying-biomass*) (e-h) tidal accretion difference between the simulation *with* mangrove drag (*drag-drying-~~biomass~~*) and the simulation *without* mangroves (*~~drag~~-drying-~~biomass~~*) (i-l) tidal accretion difference between the simulation *with* mangrove stabilisation (*~~drag~~-drying-biomass*) and the simulation *without* mangroves (*~~drag~~-drying-~~biomass~~*). [Color figure can be viewed at wileyonlinelibrary.com]

zone and forest fringe, the bed stabilisation by mangroves caused similar effects to the drag by mangroves (i.e., reduced accretion (Figure 8e,i) and increased accretion (Figure 8f,j), respectively). In the scrub forest and relict forest fringe, however, a relative increase in accretion occurred during several tidal cycles as a result of mangrove stabilisation (Figure 8k,l), indicating that mangrove stabilisation at these times increased sediment accretion, while mangrove drag reduced sediment accretion (Figure 8g,h).

4 | DISCUSSION

We developed, calibrated and validated a process-based numerical model based on field measurements from the Firth. In the discussion, we interpret the simulated mangrove forest's influence on sediment accretion patterns. Thereafter, we reflect on the model performance and assumptions. Lastly, we discuss the implications of these findings for mangrove forest development, resilience and persistence.

4.1 | Mangrove forest feedback on intertidal flat morphology

The developed model was used to determine (1) the cross-shore extent of the influence of the mangrove forests as ecosystem engineers, (2) how the magnitude and scale of this ecosystem engineering depends on hydrodynamic and sediment transport processes and (3) the relative contribution of hydrodynamic drag (due to above-ground biomass) and bed stabilisation (due to below-ground biomass) induced by mangrove trees to these ecosystem engineering effects.

These aspects were investigated by performing manipulated model simulations with and without the influence of mangrove drag and bed stabilisation (Table 2).

The model results show that the mangrove forest triggers increased accretion in the mangrove forest fringe (Figures 6 and 7). Seaward of the mangrove forest edge, in the seedling establishment zone and on the bare intertidal flat, less sediment accretes in comparison to the simulation without mangroves. The reduced accretion effect extends until an elevation between MSL and MLWN tide levels (Figure 8). Sediment from that area fronting the mangrove forest is transported further offshore than would occur in the absence of the mangrove forest, until an elevation below MLWS tide level.

Rapid sediment accretion in the forest fringe of mangrove forests has been observed in other mangrove settings in field studies (Bryan et al., 2017; Furukawa & Wolanski, 1996; Hayden & Granek, 2015; Horstman et al., 2015; Nardin et al., 2021; Van Santen et al., 2007; Willemsen et al., 2016) and model studies (Xie et al., 2020, 2022). The reduced sediment accretion in the area fronting the mangrove forest due to the mangrove presence has not been discussed in previous literature, but the effect seems to be present in the earlier bathymetric survey in the Firth (Figure 6a), showing an area with scour just seaward of the upper intertidal platform slope. The effect is initiated by the more sediment-deprived ebb flows leaving the forest (Furukawa & Wolanski 1996; Bryan et al., 2017; Mullarney et al., 2017), which entrain relatively more sediment from the area in front of the upper intertidal platform. The seaward extent of reduced sediment accretion found in this study (Figure 7b) is expected to be relatively large, because of the relatively large tidal range, wave height, tree density and suspended sediment concentrations in the Firth, in combination with the mildly sloping intertidal flat (~1:1000) (e.g., in comparison to Van Santen et al., 2007; Horstman et al., 2014; Bryan et al., 2017; Van Bijsterveldt et al., 2023). The extent of the reduced sediment accretion may also be relatively large because we considered a cross-shore section of an alongshore uniform mangrove forest, without alongshore disturbances e.g., through the presence of tidal creeks. Tidal creeks in mangrove forests steer ebb flows through the creeks (Horstman et al., 2015), and this may reduce the entrainment of sediment from the unvegetated mudflat in front of mangrove forests.

Modelled and measured processes on a tidal scale show that the volume of sediment accretion and the magnitude of the mangrove forest ecosystem engineering effects depend on the inundation depth and wave height (Figure 8) (Lovelock et al., 2015). During the highest water levels and largest waves, the upper intertidal flat platform captures the most sediment, but the ecosystem engineering effects of the mangrove forest are also the largest. These findings are in agreement with those from a recent numerical study by Xie et al. (2022), who found that the seaward slope angle of upper intertidal flat profiles may increase with tidal range and wave presence.

We found that mangrove drag (due to above-ground biomass) has a more pronounced effect on the intertidal flat morphology than mangrove stabilisation (due to below-ground biomass) (Figures 8 and 9). This finding is dependent on the attributes of the study site, including mangrove tree characteristics, and selected model parameters. In this study, mangrove drag was incorporated with drag coefficients of 3 (Supporting Information S2), while the maximum increase in τ_{cr} was 0.1 N/m^2 (Van Maanen et al., 2015). Although the type of influence on relative surface accretion/erosion between mangrove drag and bed stabilisation is similar, the effect of the bed stabilisation seems

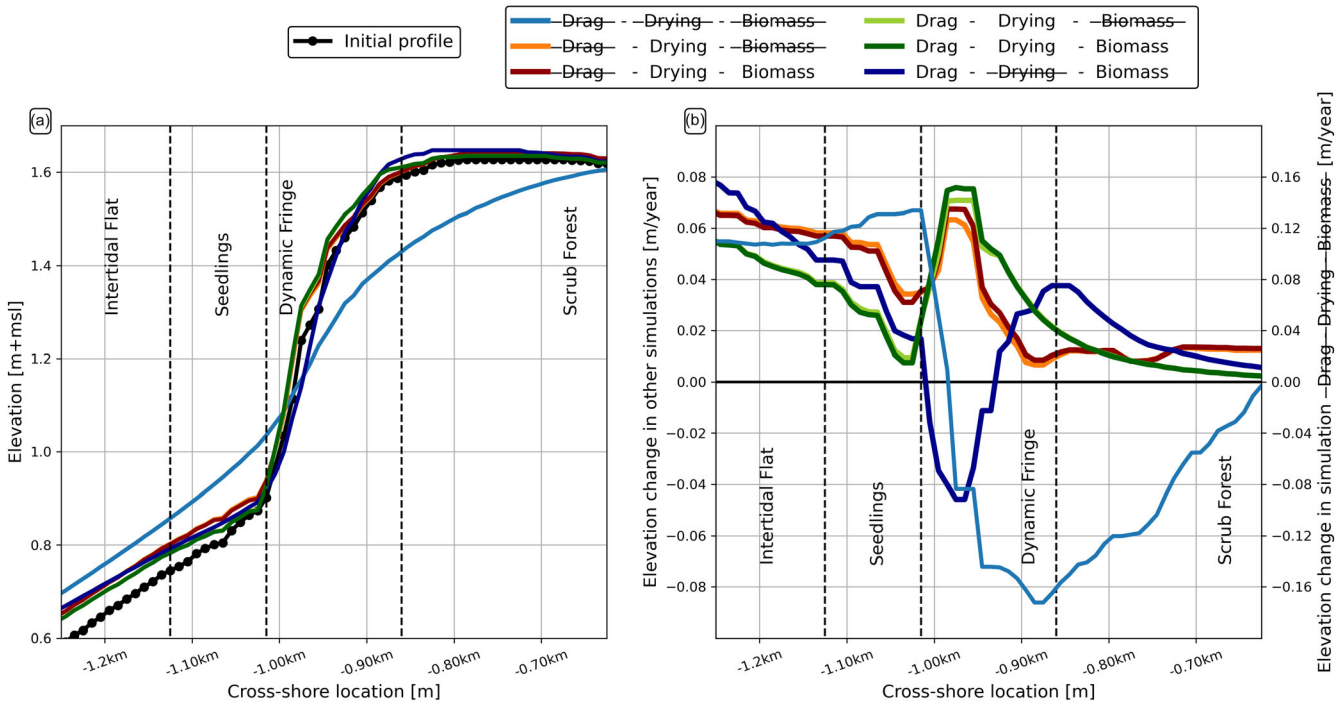

FIGURE 9 Modelled surface elevation changes for the year 2020. (a) the initial profile (January 2020) and the final profiles (January 2021) for the model simulations with the different mangrove ecosystem engineering effects (Table 2). (b) Surface elevation changes during 2020 for the model simulations with the different mangrove ecosystem engineering effects. Presented cross-shore elevation changes are median averaged over 20 m. sedimentation/accretion of *simulation* ~~*drag drying*~~ - ~~*biomass*~~ is presented on the secondary axis due to differences in magnitude compared to the other simulations. [Color figure can be viewed at wileyonlinelibrary.com]

more concentrated in the lower dynamic fringe and in the dense scrub forest (Figure 9). Mangrove drag has a more pronounced influence on the higher dynamic fringe, but no additional sediment accretion was simulated in the dense scrub forest. This cross-shore difference is caused because most of the wave attenuation by mangrove drag occurs for the highest waves in the forest fringe (Horstman et al., 2014). The bed stabilisation effect in the dense scrub forest is larger as the greatest biomass is present in that area. In the dynamic forest fringe, the bed stabilisation effect does reduce sediment entrainment, further aggravating the sediment deprivation of ebb-tidal flows that induce sediment entrainment from the unvegetated intertidal flat. We expect that the mangrove stabilisation effect gains in importance relative to the mangrove drag effect during calmer conditions (i.e. lower wave heights).

4.2 | Model performance and limitations for intertidal flat morphodynamics

The field measurements show that the importance of wind waves for transporting sediment onshore progressively increases from the subtidal to the intertidal area (i.e., with increasing elevation). While flood-dominant flow velocities induce onshore transport in the subtidal area, flow velocities become ebb dominant and induce offshore transport in the upper intertidal area closer to the mangrove forest fringe (Haughey, 2017; Lovett, 2017; Tablada Torres, 2020; Vundavilli et al., 2021). Sediment resuspension by wind waves is driven by wave dissipation and breaking, resulting in increasing *SSC* onshore in the intertidal area as well as during the initial flood and final ebb-tide phases (Green et al., 1997; Green & Coco, 2014). To accurately model these 'turbid fringes', it is essential to use a short wave computation interval. Reducing the wave computation interval to 15 minutes was crucial to simulate onshore wave-driven suspended sediment transport, due to its relation with the (tidal changes of the) water depth. Too long a wave computation interval may lead to offshore sediment transport predictions because the computed wave field may lag behind on the simulated tidal inundation depth, resulting in underpredicted wave propagation during the flood phase and overpredicted wave propagation (and sediment resuspension) during the ebb phase.

The calibrated model accurately simulates the temporal variability in water depths ($r^2 = 0.86$, rmse = 0.02 m) and cross-shore flow velocities ($r^2 = 0.75$, rmse = 0.05 m/s) at station D, but the temporal variability in suspended sediment mass is only reasonably captured for the wide range of conditions in May–June 2017 (Figure 5e,f; $r^2 = 0.44$, rmse = 0.17 kg/m^2). At station D, the overall temporal mean *SSC* (134 mg/l and 170 mg/l for measured and modelled, respectively) and standard deviation *SSC* (284 mg/l and 283 mg/l for measured and modelled, respectively) are captured well and the variability in tidal mean ($r^2 = 0.57$) and tidal maximum ($r^2 = 0.59$) are also better explained. Tidal-scale differences in *SSC* may originate from (1) the complexity in measuring *SSC*, particularly at shallow water depths and (2) model assumptions related to sediment entrainment and suspension, with time-invariable τ_{cr}, M and w_s values. Modelled sediment suspension is comparatively large during tides with lower water depths and higher waves, and comparatively small with larger water depths and smaller waves. Consequently, the type of process-based models as presented here may slightly overestimate onshore suspended sediment transport during neap tide conditions and larger waves, while underestimating onshore sediment transport during spring tide conditions and smaller waves. Spring-neap tidal scale predictions of suspended sediment transport may benefit from an *SSC*-dependent settling velocity w_s, for instance adjusting for flocculation or mud-induced turbulence damping that is not included in the model.

The model represents the monthly supply of sediment to the upper intertidal area and shows realistic accretion rates that are largest in the forest fringe (Figure 6b). The difference between the simulated net sediment accretion rate and the long-term observed surface elevation change rate was 2.5 cm/year, 1.8 cm/year, 4.4 cm/year and 2.4 cm/year at stations E, F, G and H, respectively. These differences can be attributed to subsurface elevation loss due to compaction and deep subsidence, processes that are not included in the model. Compaction is spatially variable in response to inundation depth, seasonality and vegetation density (Norris et al., 2021; Roskoden et al., 2020; Swales et al., 2016, 2019).

Surface accretion rates are underestimated by the model at stations E (5.9 cm/year) and F (2.4 cm/year) and overestimated at stations G (6.5 cm/year) and H (0.8 cm/year). At stations E and F, the difference between modelled and measured surface accretion is influenced by a substantial spatial and temporal variation, present both in the measurements and model results (Figure 6c,e). Modelled surface accretion at stations G and H (located at elevations near MHWN) may stem from the overestimation of onshore sediment transport during neap tide conditions. However, the type of models as presented here are also sensitive to the implementation of τ_{cr}. This study imposes a fixed gradient of τ_{cr} based on mean aerial exposure duration of the bed following Nguyen et al. (2020) and calibrated with measured *SSC* values in the field. The model accurately simulates the long-term profile development with realistic accretion rates. However, temporal variability due to variations in e.g., temperature, radiation, rainfall, biofilm presence or mangrove root development are not considered (Harris et al., 2016; Lelieveld et al., 2003; Nguyen et al., 2020; Nguyen et al., 2022; Pilditch et al., 2008; Stokes & Harris, 2015; Swales et al., 2019), nor is the time required for the stabilisation of freshly accreted sediment (Colosimo et al., 2023). The latter may yield an overestimated bed stability, particularly in the area where sediment accretion is largest (station G).

The complexity of determining bed stability is illustrated by a comparison between imposed τ_{cr} and measured soil shear strength (Figure 4b), which only could partly be explained with a linear fit ($p = 0.06$, $r^2 = 0.37$). This complexity stems from the spatial and temporal variability in surface sediment stability (Nguyen et al., 2022). Moreover, soil shear strength measurements in the field are not only taken at a specific point in time, they are also highly variable depending on the exact location in relation to the presence of e.g., trees, bed runnels and ponding water. The applied parameterised model based on previous studies and calibrated with field measurement data showed that the effect of aerial exposure on the sediment bed stability is the responsible mechanism for net sediment accretion in the dynamic forest fringe, and hence that bed stability must be considered to simulate the observed profile accretion in the field (Figure 9; Swales et al., 2015).

4.3 | Mangrove forest resilience and persistence

Mangroves' ecosystem engineering effects on the redistribution of sediment accretion around the mangrove forest fringe could affect longer-term intertidal flat morphology and mangrove forest development. In general, hydroperiod and sediment supply reduce with increasing surface elevation towards the upper limit of the tidal frame, followed by reduced sediment accretion rates (Figure 10a; Swales et al., 2015, 2019). In the Firth, however, sediment accretion rates increase in the dynamic fringe forest (Figures 6a,b and 10; Lovelock et al., 2010; Swales et al., 2015, 2019). Our model simulations show that the mangrove forest presence, in addition to the present morphology with increased bed stability at higher elevations due to aerial exposure, triggers additional sediment accretion on the seaward slope of the upper intertidal flat platform (Figure 6a,b). Over longer timescales, particularly with rising sea levels, this trigger could result in a more rapidly increasing surface elevation, in turn prolonging aerial exposure duration, increasing bed stability and further increasing sediment accretion rates on the seaward slope (Figure 10). However, sediment accretion rates will also reduce with increasing elevation at an elevation towards the upper tidal limit (Figure 10; Swales et al., 2015).

Contrary to the effects on the upper intertidal platform, on the unvegetated intertidal flat immediately seaward of the forest fringe, the presence of the mangrove trees triggers a reduced sediment accretion rate (Figures 7b and 9). Over longer timescales, the rate of surface elevation gain on the intertidal flat may be retarded by the presence of the mangrove forest. This effect can also influence the duration of aerial exposure and bed stability. Hence, while the mangrove forest presence may stimulate surface elevation increase in the mangrove forest fringe, it may slow down surface elevation increase on the bare intertidal flat (Figure 10).

The modelled responses of increased accretion in the fringe and reduced accretion in front of the fringe, imply that the mangrove forest may locally trigger the development of a steeper-sloped upper intertidal platform over longer timescales. This process is reflected in the existing morphology of the Firth mangroves (Figure 1b). Mangrove forests could induce a local convex-up profile shape around the forest fringe. Considering larger spatial scales, convex-up intertidal flat profiles are typically expanding and found in tide-dominated estuaries with large tidal ranges and high sediment concentrations (Friedrichs, 2011). In contrast, concave/hollow-shaped intertidal flat profiles are generally related to increased dominance of waves that cause higher bed shear stresses, sediment resuspension and erosion in upper intertidal areas (Friedrichs, 2011; Winterwerp et al., 2013).

The advance and retreat of mangrove forests have been related to the larger-scale intertidal flat morphology. In Demak, Indonesia, expanding mangrove forests have been observed on convex intertidal flats, while eroding mangrove sites were located on concave intertidal flats (Van Bijsterveldt et al., 2020, 2023). This finding is in agreement with those of model studies on wetland establishment (Hu et al., 2015). Winterwerp et al. (2013) found that the construction of seawalls in upper intertidal flats caused increased wave heights, sediment resuspension and erosion of upper intertidal flats and mangrove forests in Thailand. Mangroves along the Guyana coastline advanced in the presence of wave-sheltering mudbanks but retreated with mudbank absence (Anthony et al., 2010; Brunier et al., 2019; Proisy et al., 2009; Toorman et al., 2018). Mangroves have also been found to expand following delta expansion in East Java, Indonesia (Beselly et al., 2021) and in the Mekong Delta, Vietnam (Fricke et al., 2017). While these studies show that mangrove forests respond to larger-scale intertidal flat morphology, we found that mangrove forests may also have an active contribution to the formation of the upper

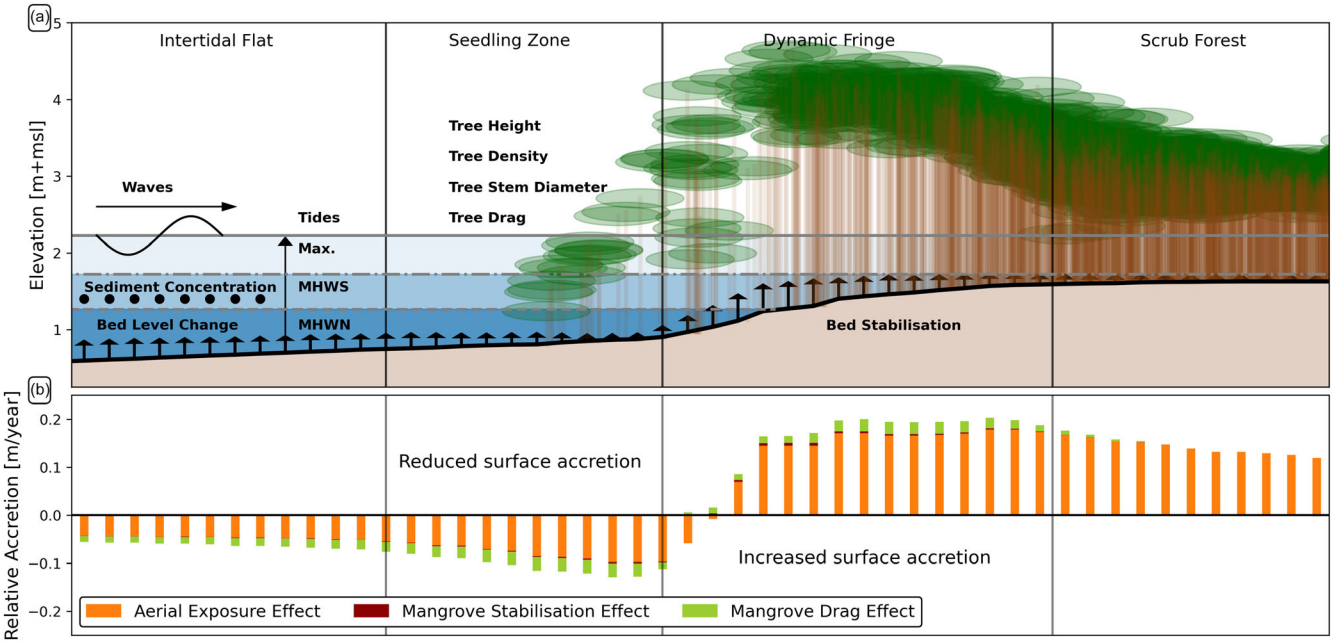

FIGURE 10 Concept of the contributions of increased bed stability due to aerial exposure, increased bed stability due to mangrove roots (below-ground biomass) and mangrove forest drag (above-ground biomass) on sediment accretion. (a) Conceptual overview of the important processes, mangrove forest zones and tree heights employed in the model. (b) Model scenario results showing results of simulations (1) *with* aerial exposure effect, (2) *with* aerial exposure and mangrove stabilisation effect, (3) *with* aerial exposure and mangrove stabilisation and drag effects. The results of the simulation *without* aerial exposure and mangrove effects are subtracted for all three scenarios. [Color figure can be viewed at wileyonlinelibrary.com]

intertidal flat morphology. This contribution will depend on mangrove forest characteristics (Bryan et al., 2017) and environmental forcing conditions (Xie et al., 2022).

Our results indicate that mangrove forests can contribute to the resilience of intertidal flats to SLR. Mangrove forests can help capturing sediment at locations higher in the cross-shore profile, thereby supporting upper intertidal platform development: i.e., wider areas with increased sediment bed stability. These stabilised vegetated upper intertidal platforms can contribute substantially to the reduction of coastal flood risk (Temmerman et al., 2023; Zhu et al., 2020). In turn, these upper intertidal platforms keep capturing the onshore transported sediment due to estuarine processes (i.e., tidal asymmetry, resuspension by waves and onshore tidal advection), even without the presence of a mangrove forest (Swales et al., 2015). With continued SLR, the presence of mangroves may cause a faster response to the increasing hydroperiod and associated potential for sediment deposition on upper intertidal flats, by increasing sediment accretion in the forest fringe, provided sufficient sediment supply (Krauss et al., 2014; Woodroffe et al., 2016). However, SLR and the associated deeper and longer tidal inundation periods also influence other processes, e.g., accommodating increased wave heights and reduced sediment bed stability due to shorter periods of aerial exposure.

In addition to enhancing the morphological resilience of upper intertidal flats, mangrove forests may influence seedling establishment conditions around the forest fringe. Mangrove colonisation opportunities typically improve with increasing surface elevation in the tidal frame, as successful mangrove seedling establishment requires a period free of tidal inundation (Balke et al., 2011). In addition, mangrove seedling establishment requires periods with limited wave forcing (Balke, Bouma, et al., 2013) and bed-level dynamics (Balke, Webb, et al., 2013). Our results imply that seedling establishment in the area fronting the existing mangrove forest is dependent on external forcing conditions (Balke et al., 2015) and rare calm weather periods (Lovelock et al., 2010; Swales et al., 2015). The mangrove forest presence itself may even slow down future forest expansion by reducing accretion on the intertidal flat. In the forest fringe, seedling establishment conditions improve by the relatively faster-increasing surface elevation as well as the reduced wave forcing and bed level dynamics (Figure 7b). Hence, our results suggest that a mangrove forest will grow rapidly once a fringe is established (De Jong et al., 2021; Nardin et al., 2016), but forest expansion first requires an external process to deposit sediment in front of the forest or trigger a seedling establishment event (Lovelock et al., 2010; Swales et al., 2015). These combined morphological and vegetation feedback mechanisms can accommodate the persistence of mangrove-vegetated intertidal flats required for their implementation in coastal flood risk reduction (Gijsman et al., 2021).

5 | CONCLUSION

Our results show that the capturing of sediment on the upper intertidal flat was predominantly influenced by the bed stability of the existing upper-intertidal morphology. This effect occurs in particular because of the prolonged aerial exposure and drying of the bed in higher elevated areas. In addition, our results show that the presence of mangrove forests can trigger increased sediment accretion in the mangrove forest fringe (i.e., up to 190 m into the forest), due to the combined drag and bed stabilisation effects of the mangrove trees. The mangrove forest presence also reduces sediment accretion in the area fronting the mangrove forest, and our model suggests that this effect is initiated by relatively larger rates of sediment entrainment due to the more sediment-deprived ebb flows leaving the forest. This effect extends 670 m seaward from the forest fringe, until an elevation below mean sea level. The length scales of these ecosystem engineering effects increase with inundation depth and wave height and are expected to reduce with lower vegetation density. Mangrove drag due to above-ground biomass is predominantly responsible for the mangrove forest effects on intertidal flat morphology. The increased bed stabilisation due to below-ground biomass has a similar but smaller contribution.

For the broader implementation of mangrove forests in coastal flood risk reduction, our results indicate that model assessment of mangrove forest persistence should consider aerial exposure effects on sediment bed stability and mangrove forest effects, in particular the mangrove drag effects (due to above-ground biomass). Our results show that, after initial establishment, mangrove forests may create favourable conditions for rapid forest fringe development, which can be beneficial for the restoration of mangrove forests or their recovery from storm impacts. Further model improvements for mangrove forest development, that are necessary for the implementation of mangroves in coastal flood risk reduction, will require seasonal to decadal-timescale data of environmental forcing conditions, bathymetric profiles and above-ground biomass changes in varying mangrove settings.

AUTHOR CONTRIBUTIONS

RG – (a) conceptualization, (c) methodology, (d) investigation, (h) writing—initial draft, (i) writing—reviewing and editing.

EMH – (a) conceptualization, (b) funding acquisition, (d) investigation, (e) resources, (g) supervision, (i) writing—reviewing and editing.

AS - (b) funding acquisition, (d) investigation, (e) resources, (i) writing—reviewing and editing.

ITM -(d) investigation, (e) resources, (i) writing—reviewing and editing.

TJB - (e) resources, (i) writing—reviewing and editing.

DvdW – (g) supervision, (i) writing—reviewing and editing.

KMW - (g) supervision, (i) writing—reviewing and editing.

ACKNOWLEDGEMENTS

The study was part of the Mangrove RESCUE project funded by the Dutch Research Council (NWO grant 15899). Contributions by AS and ITM as well as the collection of the hydrodynamic and turbidity data presented in this study are funded by the NIWA Strategic Science Investment Fund through contracts FWCE2104, FWCE2204 and CECE2304 (Estuary Sediment Dynamics and Evolution). Pressure, profile and vegetation data was partly obtained in prior field campaigns funded by the Royal Society of New Zealand's Marsden Fund (grant 14-UOW-011). The authors gratefully acknowledge colleagues from IHE Delft (Mick van der Wegen, Sebrian Beselly Putra, Johan Reyns) and Deltares (Pim Willemsen, Jasper Dijkstra, Bob Smits, Bas van Maren) for the multiple discussions that substantially contributed to the development of the model used in this study. We are grateful for the field support of Ron Ovenden (NIWA) in December 2022 in

the Firth of Thames. We acknowledge Debbie Eastwood (Waikato Regional Council) for providing the water level data from the Tararu tidal station, and NIWA for providing the wind climate data. The anonymous reviewers are gratefully acknowledged for their constructive comments that helped to improve the manuscript.

DATA AVAILABILITY STATEMENT

The profile, vegetation and ASED data that support the findings of this study are available from the corresponding author upon reasonable request. The hydrodynamic and turbidity data that support the findings of this study are available from NIWA with the permission of NIWA.

ORCID

Rik Gijsman https://orcid.org/0000-0003-3322-3262
Erik M. Horstman https://orcid.org/0000-0003-4261-1443
Andrew Swales https://orcid.org/0000-0003-1385-8017
Daphne van der Wal https://orcid.org/0000-0002-2319-056X

REFERENCES

Adame, M.F., Neil, D., Wright, S.F. & Lovelock, C.E. (2010) Sedimentation within and among mangrove forests along a gradient of geomorphological settings. *Estuarine, Coastal and Shelf Science*, 86(1), 21–30. Available from: https://doi.org/10.1016/j.ecss.2009.10.013

Anthony, E.J., Gardel, A., Gratiot, N., Proisy, C., Allison, M.A., Dolique, F., et al. (2010) The Amazon-influenced muddy coast of South America: a review of mud-bank-shoreline interactions. *Earth-Science Reviews*, 103(3-4), 99–121. Available from: https://doi.org/10.1016/j.earscirev.210.09.008

Balke, T., Bouma, T.J., Herman, P.M., Horstman, E.M., Sudtongkong, C. & Webb, E.L. (2013) Cross-shore gradients of physical disturbance in mangroves: implications for seedling establishment. *Biogeosciences*, 10(8), 5411–5419. Available from: https://doi.org/10.5194/bg-10-5411-2013

Balke, T., Bouma, T.J., Horstman, E.M., Webb, E.L., Erftemeijer, P.L.A. & Herman, P.M.J. (2011) Windows of opportunity: thresholds to mangrove seedling establishment on tidal flats. *Marine Ecology Progress Series*, 440, 1–9. Available from: https://doi.org/10.3354/meps09364

Balke, T., Swales, A., Lovelock, C.E., Herman, P.M. & Bouma, T.J. (2015) Limits to seaward expansion of mangroves: translating physical disturbance mechanisms into seedling survival gradients. *Journal of Experimental Marine Biology and Ecology*, 467, 16–25. Available from: https://doi.org/10.1016/j.jembe.2015.02.015

Balke, T., Webb, E.L., van den Elzen, E., Galli, D., Herman, P.M. & Bouma, T.J. (2013) Seedling establishment in a dynamic sedimentary environment: a conceptual framework using mangroves. *Journal of Applied Ecology*, 50(3), 740–747. Available from: https://doi.org/10.1111/1365-2664.12067

Baptist, M.J., Babovic, V., Uthurburu, J.R., Keijzer, M., Uittenbogaard, R.E., Mynett, A., et al. (2007) On inducing equations for vegetation resistance. *Journal of Hydraulic Research*, 45(4), 435–450. Available from: https://doi.org/10.1080/00221686.2007.9521778

Berger U. Hildenbrandt, H. (2000) A new approach to spatially explicit modelling of forest dynamics: spacing, ageing and neighbourhood competition of mangrove trees. *Ecological Modelling*, 132(3), 287–302. Available from: https://doi.org/10.1016/S0304-3800(00)00298-2

Beselly, S.M., van der Wegen, M., Grueters, U., Reyns, J., Dijkstra, J. & Roelvink, D. (2021) Eleven years of mangrove–mudflat dynamics on the mud volcano-induced prograding delta in East Java, Indonesia: integrating UAV and satellite imagery. *Remote Sensing*, 13(6), 1084. Available from: https://doi.org/10.3390/rs13061084

Brunier, G., Anthony, E.J., Gratiot, N. & Gardel, A. (2019) Exceptional rates and mechanisms of muddy shoreline retreat following mangrove removal. *Earth Surface Processes and Landforms*, 44(8), 1559–1571. Available from: https://doi.org/10.1002/esp.4593

Bryan, K.R., Nardin, W., Mullarney, J.C. & Fagherazzi, S. (2017) The role of cross-shore tidal dynamics in controlling intertidal sediment exchange in mangroves in Cù Lao dung. *Continental Shelf Research*, 147, 128–143. Available from: https://doi.org/10.1016/j.csr.2017.06.014

Carrasquilla-Henao, M. & Juanes, F. (2017) Mangroves enhance local fisheries catches: a global meta-analysis. *Fish and Fisheries*, 18(1), 79–93. Available from: https://doi.org/10.1111/faf.12168

Chen, R. & Twilley, R.R. (1998) A gap dynamic model of mangrove forest development along gradients of soil salinity and nutrient resources. *Journal of Ecology*, 86(1), 37–51. Available from: https://doi.org/10.1046/j.1365-2745.1998.00233.x

Colosimo, I., Van Maren, D.S., De Vet, P.L.M., Winterwerp, J.C. & Van Prooijen, B.C. (2023) Winds of opportunity: the effects of wind on intertidal flat accretion. *Geomorphology*, 439 108840. Available from: https://doi.org/10.1016/j.geomorph.2023.108840

Comley, B.W.T. & McGuiness, K.A. (2005) Above- and below-ground biomass, and allometry, of four common northern Australian mangroves. *Australian Journal of Botany*, 53(5), 431. Available from: https://doi.org/10.1071/BT04162

De Jong, S.M., Shen, Y., De Vries, J., Bijnaar, G., Van Maanen, B., Augustinus, P., et al. (2021) Mapping mangrove dynamics and colonization patterns at the Suriname coast using historic satellite data and the LandTrendr algorithm. *International Journal of Applied Earth Observation and Geoinformation*, 97, 102293. Available from: https://doi.org/10.1016/j.jag.2020.102293

Deltares. (2022a). D-flow flexible mesh-user manual. Technical report.

Deltares. (2022b). D-morphology-user manual. Technical report.

Deltares. (2022c). D-waves-user manual. Technical report.

Ezcurra, P., Ezcurra, E., Garcillán, P.P., Costa, M.T. & Aburto-Oropeza, O. (2016) Coastal landforms and accumulation of mangrove peat increase carbon sequestration and storage. *Proceedings. National Academy of Sciences. United States of America*, 113(16), 4404–4409. Available from: https://doi.org/10.1073/pnas.1519774113

Fagherazzi, S., Viggato, T., Vieillard, A., Mariotti, G. & Fulweiler, R. (2017) The effect of evaporation on the erodibility of mudflats in a mesotidal estuary. *Estuarine, Coastal and Shelf Science*, 194, 118–127. Available from: https://doi.org/10.1016/j.ecss.2017.06.011

Fricke, A.T., Nittrouer, C.A., Ogston, A.S. & Vo-Luong, H.P. (2017) Asymmetric progradation of a coastal mangrove forest controlled by combined fluvial and marine influence, Cù Lao dung, Vietnam. *Continental Shelf Research*, 147, 78–90. Available from: https://doi.org/10.1016/j.csr.2017.07.012

Friedrichs, C.T. (2011) Intertidal flat morphodynamics: a synthesis. In: Flemming, B.W. & Hansom, J.D. (Eds.) *Treatise on estuarine and coastal science: sedimentology and geology*. Elsevier, pp. 137–170 https://doi.org/10.1016/B978-0-12-374711-2.00307-7

Furukawa, K. & Wolanski, E. (1996) Sedimentation in mangrove forests. *Mangroves and Salt Mashes*, 1, 3–10. Available from: https://doi.org/10.1023/A:1025973426404

Gijsman, R., Horstman, E.M., van der Wal, D., Friess, D.A., Swales, A. & Wijnberg, K.M. (2021) Nature-based engineering: a review on reducing coastal flood risk with mangroves. *Frontiers in Marine Science*, 8, 702412. Available from: https://doi.org/10.3389/fmars.2021.702412

Gillis, L.G., Bouma, T.J., Jones, C.G., van Katwijk, M.M., Nagelkerke, I., et al. (2014) Potential for landscape-scale positive interaction among tropical marine ecosystems. *Marine Ecology Progress Series*, 503, 289–303. Available from: https://doi.org/10.3354/meps10716

Glover, H.E., Stokes, D.J., Ogston, A.S., Bryan, K.R. & Pilditch, C.A. (2022) Decadal-scale impacts of changing mangrove extent on hydrodynamics and sediment transport in a quiescent, mesotidal estuary. *Earth Surface Processes and Landforms*, 1–17(5), 1287–1303. Available from: https://doi.org/10.1002/esp.5317

Green, M.O., Black, K.P. & Amos, C.L. (1997) Control of estuarine sediment dynamics by interactions between currents and waves at several scales. *Marine Geology*, 144(1-3), 97–116. Available from: https://doi.org/10.1016/S0025-3227(97)00065-0

Green, M.O. & Coco, G. (2014) Review of wave-driven sediment resuspension and transport in estuaries. *Reviews of Geophysics*, 52(1), 77–117. Available from: https://doi.org/10.1002/2013RG000437

Harris, R.J., Pilditch, C.A., Greenfield, B.L., Moon, V. & Kröncke, I. (2016) The influence of benthic macrofauna on the erodibility of intertidal sediments with varying mud content in three New Zealand estuaries. *Estuaries and Coasts*, 39(3), 815–828. Available from: https://doi.org/10.1007/s12237-015-0036-2

Haughey, R.R. (2017) *Modelling the hydrodynamics within the mangrove tidal flats in the firth of Thames*. MSc thesis,. New Zealand: The University of Waikato.

Hayden, H.L. & Granek, E.F. (2015) Coastal sediment elevation change following anthropogenic mangrove clearing. *Estuarine, Coastal and Shelf Science*, 165, 70–74. Available from: https://doi.org/10.1016/j.ecss.2015.09.004

Horstman, E.M., Bryan, K.R. & Mullarney, J.C. (2021) Drag variations, tidal asymmetry and tidal range changes in a mangrove creek system. *Earth Surface Processes and Landforms*, 1–19(9), 1828–1846. Available from: https://doi.org/10.1002/esp.5124

Horstman, E.M., Dohmen-Janssen, C.M., Bouma, T.J. & Hulscher, S.J.M.H. (2015) Tidal-scale flow routing and sedimentation in mangrove forests: combining field data and numerical modelling. *Geomorphology*, 228, 244–262. Available from: https://doi.org/10.1016/j.geomorph.2014.08.011

Horstman, E.M., Dohmen-Janssen, C.M., Narra, P.M., van den Berg, N.J., Siemerink, M. & Hulscher, S.J. (2014) Wave attenuation in mangroves: a quantitative approach to field observations. *Coastal Engineering*, 94, 47–62. Available from: https://doi.org/10.1016/j.coastaleng.2014.08.005

Horstman, E.M., Lundquist, C.J., Bryan, K.R., Bulmer, R.H., Mullarney, J.C. & Stokes, D.J. (2018) In: Makowski, C. & Finkl, C. (Eds.) *"The dynamics of expanding mangroves in New Zealand," in threats to mangrove forests. Coastal research library*, Vol. 25. Cham: Springer. https://doi.org/10.1007/978-3-319-73016-5_2

Hu, Z., van Belzen, J., van der Wal, D., Balke, T., Wang, Z.B., Stive, M., et al. (2015) Windows of opportunity for salt marsh vegetation establishment on bare intertidal flats: the importance of tempora land spatial variability in hydrodynamic forcing. *Journal of Geophysical Research – Biogeosciences*, 120(7), 1450–1469. Available from: https://doi.org/10.1002/2014JG002870

Huxham, M., Kumara, M.P., Jayatissa, L.P., Krauss, K.W., Kairo, J., Langat, J., et al. (2010) Intra- and interspecific facilitation in mangroves may increase resilience to climate change threats. *Phil Trans. R. Soc. B Biol. Sci.*, 365(1549), 2127–2135. Available from: https://doi.org/10.1098/rstb.2010.0094

Krauss, K.W., Allen, J.A. & Cahoon, D.R. (2003) Differential rates of vertical accretion and elevation change among aerial root types in Micronesian mangrove forests. *Estuarine, Coastal and Shelf Science*, 56(2), 251–259. Available from: https://doi.org/10.1016/S0272-7714(02)00184-1

Krauss, K.W., Mckee, K.L., Lovelock, C.E., Cahoon, D.R., Saintilan, N., Reef, R., et al. (2014) How mangrove forests adjust to rising sea level. *The New Phytologist*, 202(1), 19–34. Available from: https://doi.org/10.1111/nph.12605

Lelieveld, S.D., Pilditch, C.A. & Green, M.O. (2003) Variation in sediment stability and relation to indicators of microbial abundance in the Okura estuary, New Zealand. *Estuarine, Coastal and Shelf Science*, 57(1-2), 123–136. Available from: https://doi.org/10.1016/S0272-7714(02)00336-0

Lovelock, C.E., Adame, M.F., Bennion, V., Hayes, M., Reef, R., Santini, N., et al. (2015) Sea level and turbidity controls on mangrove soil surface elevation change. *Estuarine, Coastal and Shelf Science*, 153, 1–9. Available from: https://doi.org/10.1016/j.ecss.2014.11.026

Lovelock, C.E., Sorrell, B.K., Hancock, N., Hua, Q. & Swales, A. (2010) Mangrove forest and soil development on a rapidly accreting shore in New Zealand. *Ecosystems*, 13(3), 437–451. Available from: https://doi.org/10.1007/s10021-010-9329-2

Lovett, N.J. (2017) *Sediment transport in the firth of Thames mangrove forest, New Zealand*. MSc thesis,. New Zealand: The University of Waikato.

Mazda, Y., Magi, M., Ikeda, Y. et al. Wave reduction in a mangrove forest dominated by Sonneratia sp. *Wetlands Ecol Manage* 14, 365–378 (2006). https://doi.org/10.1007/s11273-005-5388-0

Mazda, Y. & Wolanski, E. (2009) Hydrodynamics and modelling of water flow in mangrove areas. In: Perillo, G.M.E., Wolanski, E., Cahoon, D.-R. & Brinson, M.M. (Eds.) *Coastal wetlands: an integrated ecosystem approach*. Amsterdam, The Netherlands: Elsevier, pp. 231–261.

Mendez, F.J. & Losada, I.J. (2004) An empirical model to estimate the propagation of random breaking and nonbreaking waves over vegetation fields. *Coastal Engineering*, 51(2), 103–118. Available from: https://doi.org/10.1016/j.coastaleng.2003.11.003

Montgomery, J.M., Bryan, K.R., Horstman, E.M. & Mullarney, J.C. (2018) Attenuation of tides and surges by mangroves: contrasting case studies from New Zealand. *Watermark*, 10(9), 1119. Available from: https://doi.org/10.3390/w10091119

Montgomery, J.M., Bryan, K.R., Mullarney, J.C. & Horstman, E.M. (2019) Attenuation of storm surges by coastal mangroves. *Geophysical Research Letters*, 46(5), 2680–2689. Available from: https://doi.org/10.1029/2018GL081636

Mullarney, J.C., Henderson, S.M., Reyns, J.A.H., Norris, B.K. & Bryan, K.R. (2017) Spatially varying drag within a wave-exposed mangrove forest and on the adjacent tidal flat. *Continental Shelf Research*, 147, 102–113. Available from: https://doi.org/10.1016/j.csr.2017.06.019

Nardin, W., Locatelli, S., Pasquarella, V., Rulli, M.C., Woodcock, C.E. & Fagherazzi, S. (2016) Dynamics of a fringe mangrove forest detected by Landsat images in the Mekong River Delta, Vietnam. *Earth Surface Processes and Landforms*, 41(14), 2024–2037. Available from: https://doi.org/10.1002/esp.3968

Nardin, W., Vona, I. & Fagherazzi, S. (2021) Sediment deposition affects mangrove forests in the Mekong delta, Vietnam. *Continental Shelf Research*, 213, 104319. Available from: https://doi.org/10.1016/j.csr.2020.104319

Nguyen, H.M., Bryan, K.R. & Pilditch, C.A. (2020) The effect of long-term aerial exposure on intertidal mudflat erodibility. *Earth Surface Processes and Landforms*, 45(14), 3623–3638. Available from: https://doi.org/10.1002/esp.4990

Nguyen, H.M., Bryan, K.R., Pilditch, C.A. & Moon, V.G. (2019) Influence of ambient temperature on erosion properties of exposed cohesive sediment from an intertidal mudflat. *Geo-Marine Letters*, 39(4), 337–347. Available from: https://doi.org/10.1007/s00367-019-00579-x

Nguyen, H.M., Bryan, K.R., Zhou, Z. & Pilditch, C.A. (2022) Modeling the effects of aerial temperature and exposure period on intertidal mudflat profiles. *Continental Shelf Research*, 245, 104802. Available from: https://doi.org/10.1016/j.csr.2022.104802

Norris, B.K., Mullarney, J.C., Bryan, K.R. & Henderson, S.M. (2021) Relating millimeter-scale turbulence to meter-scale subtidal erosion and accretion across the fringe of a coastal mangrove forest. *Earth Surface Processes and Landforms*, 46(3), 573–592. Available from: https://doi.org/10.1002/esp.5047

Partheniades, E. (1965) Erosion and deposition of cohesive soils. *Journal of the Hydraulics Division*, 91(1), 105–139. Available from: https://doi.org/10.1061/jyceaj.0001165

Pilditch, C.A., Widdows, J., Kuhn, N.J., Pope, N.D. & Brinsley, M.D. (2008) Effects of low tide rainfall on the erodibility of intertidal cohesive sediments. *Continental Shelf Research*, 28(14), 1854–1865. Available from: https://doi.org/10.1016/j.csr.2008.05.001

Proisy, C., Gratiot, N., Anthony, E.J., Gardel, A., Fromard, F. & Heuret, P. (2009) Mud bank colonization by opportunistic mangroves: a case study from French Guiana using lidar data. *Continental Shelf Research*, 29(3), 632–641. Available from: https://doi.org/10.1016/j.csr.2008.09.017

Roskoden, R.R., Bryan, K.R., Schreiber, I. & Kopf, A. (2020) Rapid transition of sediment consolidation across an expanding mangrove fringe in the firth of Thames New Zealand. *Geo-Marine Letters*, 40(2), 295–308. Available from: https://doi.org/10.1007/s00367-019-00589-9

Stokes, D.J. & Harris, R.J. (2015) Sediment properties and surface erodibility following a large-scale mangrove (Avicennia marina) removal. *Continental Shelf Research*, 107, 1–10. Available from: https://doi.org/10.1016/j.csr.2015.07.011

Swales, A., Bentley, S.J. & Lovelock, C.E. (2015) Mangrove-forest evolution in a sediment-rich estuarine system: opportunists or agents of geomorphic change. *Earth Surface Processes and Landforms*, 40(12), 1672–1687. Available from: https://doi.org/10.1002/esp.3759

Swales, A., Denys, P., Pickett, V.I. & Lovelock, C.E. (2016) Evaluating deep subsidence in a rapidly-accreting mangrove forest using GPS monitoring of surface-elevation benchmarks and sedimentary records. *Marine Geology*, 380, 205–218. Available from: https://doi.org/10.1016/j.margeo.2016.04.015

Swales, A., Reeve, G., Cahoon, D.R. & Lovelock, C.E. (2019) Landscape evolution of a fluvial sediment-rich *Avicennia marina* mangrove forest: insights from seasonal and inter-annual surface-elevation dynamics. *Ecosystems*, 22(6), 1232–1255. Available from: https://doi.org/10.1007/s10021-018-0330-5

Tablada Torres, J.J. (2020) *Suspended sediment transport processes on a wave-exposed tidal flat in the southern firth of Thames*. MSc thesis,. New Zealand: the University of Auckland.

Temmerman, S., Horstman, E.M., Krauss, K.W., Mullarney, J.C., Pelckmans, I. & Schoutens, K. (2023) Marshes and mangroves as nature-based coastal storm buffers. *Annual Review of Marine Science*, 15(1), 95–118. Available from: https://doi.org/10.1146/annurev-marine-040422-092951

Toorman, E., Anthony, E.J., Augustinus, P.G.E.F., Gardel, A., Gratiot, N., Homenauth, O., et al. (2018) Interaction of mangroves, coastal hydrodynamics and morphodynamics along the coastal fringes of the Guianas. *Coastal Research Library*, 25, 429–473. Available from: https://doi.org/10.1007/978-3-319-73016-5_20

Van Bijsterveldt, C.E.J., Van der Wal, D., Gijon Mancheno, A., Fivash, G.S., Helmi, M. & Bouma, T.J. (2023) Can cheniers protect mangroves along eroding coastlines? – the effect of contrasting foreshore types on mangrove stability. *Ecological Engineering*, 187, 106863. Available from: https://doi.org/10.1016/j.ecoleng.2022.106863

van Bijsterveldt, C.E.J., van Wesenbeeck, B.K., van der Wal, D., Afiati, N., Pribadi, R., Brown, B., et al. (2020) How to restore mangroves for greenbelt creation along eroding coasts with abandoned aquaculture ponds. *Estuarine, Coastal and Shelf Science*, 235, 106576. Available from: https://doi.org/10.1016/j.ecss.2019.106576

Van de Koppel, J., van der Heide, T., Altieri, A.H., Eriksson, B.K., Bouma, T.J., Olff, H., et al. (2015) Long-distance interactions regulate the structure and resilience of coastal ecosystems. *Annual Review of Marine Science*, 7(1), 139–158. Available from: https://doi.org/10.1146/annurev-marine-010814-015805

Van Maanen, B., Coco, G. & Bryan, K.R. (2015) On the ecogeomorphological feedbacks that control tidal channel network evolution in a sandy mangrove setting. *Proc. R. Soc. a Math. Phys. Eng. Sci.*, 471, 20150115. Available from: https://doi.org/10.1098/rspa.2015.0115

Van Santen, P., Augustinus, P.G.E.F., Janssen-Stelder, B.M., Quartel, S. & Tri, N.H. (2007) Sedimentation in an estuarine mangrove system. *Journal of Asian Earth Sciences*, 29(4), 566–575. Available from: https://doi.org/10.1016/j.jseaes.2006.05.011

Vundavilli, H., Mullarney, J.C., MacDonald, I.T. & Bryan, K.R. (2021) The interaction of buoyant coastal river plumes with mangrove vegetation and consequences for sediment deposition and erosion in a tidal environment. *Continental Shelf Research*, 222, 104417. Available from: https://doi.org/10.1016/j.csr.2021.104417

Willemsen, P.W., Horstman, E.M., Borsje, B.W., Friess, D.A. & Dohmen-Janssen, C.M. (2016) Sensitivity of the sediment trapping capacity of an estuarine mangrove forest. *Geomorphology*, 273, 189–201. Available from: https://doi.org/10.1016/j.geomorph.2016.07.038

Willemsen, P.W.J.M., Horstman, E.M., Bouma, T.J., Baptist, M.J., van Puijenbroek, M.E.B. & Borsje, B.W. (2022) Facilitating salt marsh restoration: the importance of event-based bed level dynamics and seasonal trends in bed level change. *Frontiers in Marine Science*, 8, 793235. Available from: https://doi.org/10.3389/fmars.2021.793235

Willemsen, P.W.J.M., Smits, B.P., Borsje, B.W., Herman, P.M.J., Dijkstra, J.T., Bouma, T.J., et al. (2022) Modeling decadal salt marsh development: variability of the salt marsh edge under influence of waves and sediment availability. *Water Resources Research*, 58(1), e2020WR028962. Available from: https://doi.org/10.1029/2020WR028962

Winterwerp, J.C., Erftemeijer, P.L., Suryadiputra, N., Van Eijk, P. & Zhang, L. (2013) Defining eco-morphodynamic requirements for rehabilitating eroding mangrove-mud coasts. *Wetlands*, 33(3), 515–526. Available from: https://doi.org/10.1007/s13157-013-0409-x

Woodroffe, C.D., Rogers, K., McKee, K.L., Lovelock, C.E., Mendelssohn, I.A. & Saintilan, N. (2016) Mangrove sedimentation and response to relative sea-level rise. *Annual Review of Marine Science*, 8(1), 243–266. Available from: https://doi.org/10.1146/annurev-marine-122414-034025

Worthington, T.A., Zu Ermgassen, P.S., Friess, D.A., Krauss, K.W., Lovelock, C.E., Thorley, J., et al. (2020) A global biophysical typology of mangroves and its relevance for ecosystem structure and deforestation. *Scientific Reports*, 10(1), 14652. Available from: https://doi.org/10.1038/s41598-020-71194-5

Xie, D., Schwarz, C., Bruckner, M.Z.M., Kleinhans, M.G., Urrego, D.H., Zhou, Z., et al. (2020) Mangrove diversity loss under sea-level rise triggered by bio-morphodynamic feedbacks and anthropogenic pressures. *Environmental Research Letters*, 15(11), 114033.

Xie, D., Schwarz, C., Kleinhans, M.G., Zhou, Z. & van Maanen, B. (2022) Implications of coastal conditions and sea-level rise on mangrove vulnerability: a bio-morphodynamic modeling study. *Journal of Geophysical Research - Earth Surface*, 127(3), e2021JF006301. Available from: https://doi.org/10.1029/2021JF006301

Zhu, Z., Vuik, V., Visser, P.J., Soens, T., van Wesenbeeck, B., van de Koppel, J., et al. (2020) Historic storms and the hidden value of coastal wetlands for nature-based flood defence. *Nat. Sustain.*, 3(10), 853–862. Available from: https://doi.org/10.1038/s41893-020-0556-z

SUPPORTING INFORMATION

Additional supporting information can be found online in the Supporting Information section at the end of this article.

How to cite this article: Gijsman, R., Horstman, E.M., Swales, A., MacDonald, I.T., Bouma, T.J., van der Wal, D. et al. (2024) Mangrove forest drag and bed stabilisation effects on intertidal flat morphology. *Earth Surface Processes and Landforms*, 49(3), 1117–1134. Available from: https://doi.org/10.1002/esp.5758